Palaeogeography, Palaeoclimatology, Palaeoecology 548 (2020) 109668

Contents lists available at ScienceDirect

Palaeogeography, Palaeoclimatology, Palaeoecology

journal homepage: www.elsevier.com/locate/palaeo

High-precision U-Pb zircon age constraints on the Guadalupian in West Texas, USA

Qiong Wu[a,b], Jahandar Ramezani[d], Hua Zhang[a], Dong-xun Yuan[a], Douglas H. Erwin[e], Charles M. Henderson[f], Lance L. Lambert[g], Yi-chun Zhang[a], Shu-zhong Shen[c,*]

[a] Nanjing Institute of Geology and Palaeontology, Chinese Academy of Sciences, Nanjing 210008, China
[b] University of Science and Technology of China, Hefei 230026, China
[c] School of Earth Sciences and Engineering, Nanjing University, 163 Xianlin Avenue, Nanjing 210023, China
[d] Department of Earth, Atmospheric and Planetary Sciences, Massachusetts Institute of Technology, Cambridge, MA 02139, USA
[e] Department of Paleobiology, MRC-121, National Museum of Natural History, Washington, D.C. 20013-7012, USA
[f] Department of Geoscience, University of Calgary, Calgary, AB T2N 1N4, Canada
[g] Department of Geological Sciences, University of Texas at San Antonio, One UTSA Circle, San Antonio, TX 78249, USA

ARTICLE INFO

Editor: F Zhang

Keywords:
Zircon U-Pb geochronology
Bayesian model
Mass extinction
Emeishan Large Igneous Province
Conodont biostratigraphy
Illawarra Reversal

ABSTRACT

The Guadalupian Epoch was characterized by major changes in paleogeography, paleoclimate, and biodiversity. Yet, the paucity of precise and accurate radioisotopic dates from the Guadalupian stages in their type area, Guadalupe Mountains National Park in West Texas has rendered their calibration inadequate. In this study, we report high-precision U-Pb zircon geochronology by the CA-ID-TIMS method from three ash beds (2σ internal errors only) in the Rader Member of the Bell Canyon Formation at the Back Ridge Section (262.127 ± 0.097 Ma, MSWD = 0.89, n = 3), the lower Pinery Member of the Bell Canyon Formation at the Frijole Section (264.23 ± 0.13 Ma, MSWD = 0.89, n = 8) and the basal South Wells Member of the Cherry Canyon Formation at the Monolith Canyon Section (266.525 ± 0.078 Ma, MSWD = 0.62, n = 5). The Bayesian interpolation statistics method is used to establish an age-stratigraphy model that estimates the base of the Capitanian to be 264.28 ± 0.16 Ma, serving as the best age estimate for the Capitanian Stage at present. In addition, we review the existing geochronology from the Guadalupian Series in West Texas and seek to propose more precise temporal estimates of Guadalupian geological and biological events. These data constrain the high-frequency sequences of the Cherry Canyon and Bell Canyon formations in the Guadalupe Mountains National Park area. Accordingly, the base of the Wordian is estimated at 266.9 ± 0.4 Ma and the Illawarra geomagnetic polarity reversal in West Texas at 267.4 ± 0.4 Ma to 266.5 ± 0.3 Ma. The global end-Guadalupian extinction began in the conodont zone of *Jinogondolella altudaensis* above the base of the Reef Trail Member of the Bell Canyon Formation and might continue to the *Clarkina postbitteri postbitteri* Zone in the earliest Wuchiapingian. The conodonts display a rapid evolutionary rate during this interval. This constrains the biotic crisis from *ca.* 260 Ma to 259 Ma based on our conodont age estimation. The emplacement of the Emeishan Large Igneous Province (ELIP) in South China has been constrained to *ca.* 260 Ma to 257.4 Ma based on zircon U-Pb geochronology by the CA-ID-TIMS method, overlapping with the end-Guadalupian extinction, which provides support for the temporal relationship between them. Additionally, the ELIP persisted into the early Wuchiapingian and may have hampered ecosystem restoration during the post-extinction interval.

1. Introduction

The Guadalupian (Middle Permian) interval is characterized by major changes in paleogeography, paleoclimate, and biodiversity that remain poorly calibrated in time. The major changes include the: initial breakup of the supercontinent Pangea (Isozaki, 2009), largest global regression during the Paleozoic (Haq and Schutter, 2008), termination of the Late Paleozoic Ice Age (Fielding et al., 2008; Chen et al., 2013; Montañez and Poulsen, 2013), seawater temperature fluctuations from the late Guadalupian to the Wuchiapingian (Isozaki et al., 2007, 2011; Chen et al., 2011, 2013), fluctuations in marine carbon cycle (Isozaki et al., 2007; Wignall et al., 2009a; Bond et al., 2010b; Cao et al., 2018;

* Corresponding author.
E-mail address: szshen@nju.edu.cn (S.-z. Shen).

https://doi.org/10.1016/j.palaeo.2020.109668
Received 13 January 2020; Received in revised form 9 February 2020; Accepted 10 February 2020
Available online 19 February 2020

Yang et al., 2018), decline in seawater strontium isotope composition to their lowest point during the Permian (Korte et al., 2006; Kani et al., 2013; Wang et al., 2018; Biakov et al., 2019), and the emplacement of the Emeishan Large Igneous Province (ELIP) across the Guadalupian-Lopingian boundary (GLB) in South China (Zhou et al., 2002; He et al., 2007). The ELIP has long been considered as a potential cause of the end-Guadalupian or pre-Lopingian biotic crisis (Jin et al., 1994; Stanley and Yang, 1994; Zhou et al., 2002; Wignall et al., 2009a; Bond et al., 2010a, 2010b). A high-resolution geochronologic framework is necessary to assess timings and rates of changes in order to evaluate causal relationships among these events. Existing high-precision radioisotopic dates have been insufficient to establish a temporal framework at the desired resolution for the Guadalupian.

Major advances in radioisotopic age analyses together with newly discovered interbedded tuffs suitable to geochronology have greatly improved the precision and accuracy of the Permian timescale over the last two decades. However, these improvements have largely been limited to the Cisuralian stages in the southern Urals (Ramezani et al., 2007; Schmitz and Davydov, 2012) and the Lopingian stages in South China, especially the interval from the end-Permian mass extinction to the Early Triassic recovery (Shen et al., 2011, 2019a; Burgess et al., 2014; Baresel et al., 2017). For a considerable time there has been only one direct high-precision radioisotopic date from the *ca.* 30 myr interval spanning the late Cisuralian to the end of the Guadalupian (Ramezani and Bowring, 2018). Consequently, the late Cisuralian to end-Guadalupian calibrations of the international geologic timescale (*e.g.*, Henderson et al., 2012; Ramezani and Bowring, 2018; Shen et al., 2019b) had to be indirectly extrapolated.

Although several volcanic ash beds were identified from Guadalupian successions in the type area in West Texas, USA, most studies focused on their correlations based on geochemical characteristics, with only few reported radioisotopic dates in support of these correlations (King, 1948; Nicklen et al., 2015a, 2015b). Several Guadalupian high-precision U-Pb dates by the chemical abrasion isotope dilution thermal ionization mass spectrometry (CA-ID-TIMS) method have been reported from regions far away from the West Texas type area, including dates from South China and Japan in the Tethyan realm (Wu et al., 2017; Davydov and Schmitz, 2019), Russia in the northern high-latitudes (Davydov et al., 2016, 2018b) and Australia in the southern (Gondwanan) high-latitudes (Metcalfe et al., 2015; Laurie et al., 2016). However, because of strong faunal provincialism it is difficult to apply these dates to the global Guadalupian time scale. This continues to hamper biostratigraphic correlations between the Tethyan realm and the type area. Additionally, most of the dates from Australia and Russia are from terrestrial successions with endemic fossils and ambiguous correlations to the marine-based geologic time scale.

To address the absence of a robust chronostratigraphy from the type area, extensive fieldwork to identify additional ash beds with potential for high-precision U-Pb zircon dating was conducted in Guadalupe Mountains National Park (GMNP) in West Texas, USA, with dozens of biostratigraphically constrained new samples added to the collection (Fig. 1C; Table 1). This study reports three new high-precision U-Pb zircon dates by the CA-ID-TIMS technique from GMNP that span the key upper Wordian to lower Capitanian interval. In combination with a review of the existing geochronology, we discuss implications for Guadalupian geologic and biologic events.

2. Geologic setting and stratigraphy

The Guadalupian Series is composed of the Roadian, Wordian and Capitanian stages in ascending order (Glenister et al., 1992, 1999; Jin et al., 1997). The Global Stratotype Section and Points (GSSPs) of all three stages, as defined by conodont biostratigraphy, were selected from the basinal to lower slope carbonate successions along the northwestern margin of the Permian Delaware Basin in GMNP, West Texas, USA (Fig. 1; Glenister et al., 1999). The stratigraphy of the type area consists of the Cutoff, Brushy Canyon, Cherry Canyon, and Bell Canyon formations in ascending order. The Cutoff Formation is characterized by predominately carbonate, and thickens towards the basin. The overlying three formations are generally characterized in basinal settings by siliciclastic deposits interbedded with limestone beds (members), which tend to thin out from the toe-of-slope towards the basin. The Bell Canyon Formation is overlain by the Castile Formation, characterized by up to 600 m of evaporites and roughly dated to Late Permian (Becker et al., 2002; Roberts et al., 2017). The base of the Roadian Stage is defined by the first appearance datum (FAD) of the conodont *Jinogondolella nankingensis* in the middle of the El Centro Member of the Cutoff Formation at the Stratotype Canyon Section; the base of the Wordian Stage by the FAD of *J. aserrata* in the upper Getaway Limestone Member of the Cherry Canyon Formation at the Gateway Ledge Section; and the base of the Capitanian Stage by the FAD of *J. postserrata* in the lower Pinery Limestone Member of the Bell Canyon Formation at the Nipple Hill Section (Fig. 3; Glenister et al., 1999; Mei et al., 2002; Henderson et al., 2012). The global correlation of the Guadalupian Series is mainly based on conodont, fusulinid and ammonoid biostratigraphy.

Guadalupian rocks crop out along the Guadalupe, Delaware, Apache, and Glass Mountains regions in the Delaware Basin in West Texas, which were located in an equatorial area of the western margin of Pangea during the Guadalupian (Fig. 1; Glenister et al., 1992). Our study of the base Capitanian focused on the area around Nipple Hill close to US Highway 62/180, which is the GSSP of the Capitanian Stage with good Wordian to Capitanian outcrops (Fig. 2). As only a half meter of strata is preserved above the Capitanian GSSP at the Nipple Hill Section (Fig. 2C), the Frijole Section in effect provides an upward extension of the Capitanian succession above the GSSP.

The Monolith Canyon Section (31°54′44.37″N, 104°46′56.58″W) is located in a drainage northeast of the Nipple Hill Section (Fig. 2), where the South Wells Member of the Cherry Canyon Formation is well exposed. The South Wells Member is characterized by a group of less resistant and more discontinuous limestone beds. These limestone beds pinch out and are replaced by thick sandstones near the area east of Nipple Hill (King, 1948). The exposed strata at the Monolith Canyon Section are mainly composed of sandstones and black shales interbedded with three tuff/tuffaceous beds (Fig. 2D). The bentonite in the basal part of the South Wells Member has yielded one of the high-precision U-Pb zircon dates of this study.

The Frijole Section (31°54′15.09″N, 104°49′12.93″W) exposes the uppermost Cherry Canyon Formation and the lower Bell Canyon Formation in steep outcrops near the Capitan forereef (Fig. 2). The succession is mainly composed of limestones, limestones with chert nodules, sandstones, mudstones, and subordinate shales. The location and lithostratigraphy of the newly measured Frijole Section are in good agreement with the sections to the north and northwest of Nipple Hill described by King (1948) (*e.g.*, Sections 21, 23, 64, 65, 66 and 67). Following King (1948), we identify the uppermost Manzanita Member limestones of the Cherry Canyon Formation and the lowermost Hegler Member limestones of the Bell Canyon Formation near the base of the Frijole Section (Fig. 2A). These limestone beds are interbedded with thin sandstone and siltstone beds and occur *ca.* 15 m below the base of the Pinery Member at the Frijole Section. A thin bentonite bed 7.4 m above the base of the Pinery Member (Bell Canyon Formation) at this section has yielded a U-Pb zircon age that is used here to further constrain the Wordian-Capitanian boundary.

The correlation of the Frijole Section strata to the Nipple Hill GSSP is complicated by generally poor exposure below the Pinery Member at the two sections. Although the basal limestones at the Nipple Hill Section can be reliably assigned to the Manzanita Member based on the correlation of the ash beds, the correlation of a *ca.* 4 meters-thick silty carbonate interval about 15 m higher at this section (Fig. 2) to the Hegler Member has been controversial (Nicklen et al., 2015b). Whether the mid-section carbonate layer of the Nipple Hill Section correlates

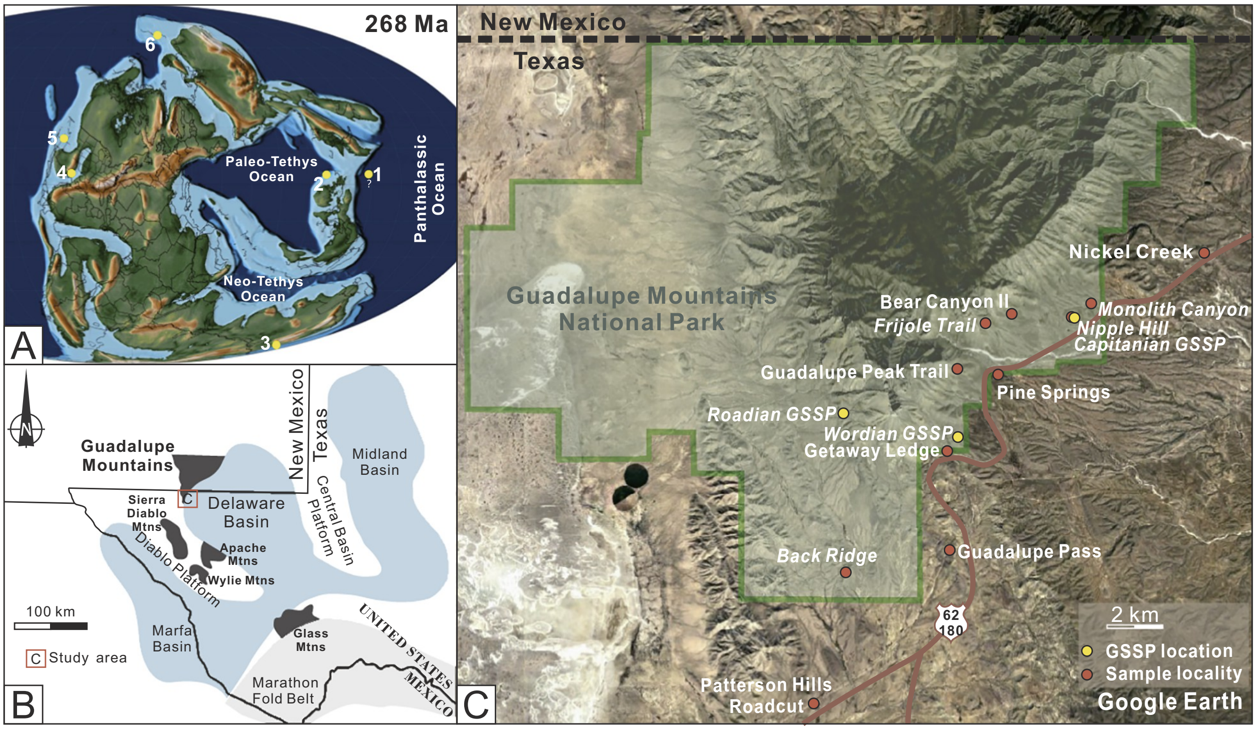

Fig. 1. (A) Middle Permian (*ca.* 268 Ma) global paleogeography from Scotese (2014) marked with regions (filled circles) of the Guadalupian dates that discussed in this study. 1-Akiyoshi, Japan (Kasuya et al., 2012; Davydov and Schmitz, 2019); 2-Chaohu, South China (Wu et al., 2017); 3-Sydney Basin, Australia (Metcalfe et al., 2015; Laurie et al., 2016; Belica et al., 2017); 4-Delaware Basin, USA (Ramezani and Bowring, 2018; this study); 5-Phosphoria Basin, USA (Davydov et al., 2018a); 6-Okhotsk Basin, Russia (Davydov et al., 2016, 2018b). (B) Location of the study area in the Delaware Basin in West Texas, USA modified from Glenister et al. (1992). (C) Guadalupe Mountains National Park area marked with the localities of the tuff and tuffaceous samples and Guadalupian GSSPs.

with the Hegler Member or the topmost Manzanita Member will make the lower part of the Frijole Section more expanded or condensed relative to the Nipple Hill GSSP. However, this will have a minimal impact on the stage boundary age interpolation as the base of the Pinery Member cherty limestones is well correlated between the two sections. In addition, the Hegler Member is relatively thin with a thickness of less than 5 m around the Nipple Hill area (King, 1948). The Pinery Member has a thickness of about 60 m to 80 m at the Frijole Section and it is overlain by the Rader Member. The Rader Member is a thick-bedded limestone, with some of beds containing angular limestone cobbles (King, 1948).

The locality known as Back Ridge (31°49′28.11″N, 104°52′32.95″W) in the Paterson Hills area of GMNP to the south of Guadalupe Peak (Figs. 1 and 2B) has exposed another tuff bed that has successfully produced an additional U-Pb age constraint for the Capitanian Stage. This tuff occurs near the top of the exposed section and in the Rader Member of the Bell Canyon Formation that overlies the Pinery Member at the Back Ridge Section.

3. U-Pb zircon geochronology

In excess of 20 samples identified as bentonite or tuffaceous sedimentary rock were collected from the Wordian and Capitanian strata of the Delaware Basin in GMNP, Texas as part of this study (Table 1). Only a few yielded zircons of volcanic origin suitable for ash bed geochronology.

3.1. Analytical methods

The three geochronology samples of this study were between 3.0 kg and 9.15 kg in weight and were processed by soaking in water for 48 h, followed by gradual disaggregation and removal of the clay-rich fraction in a sonic dismembrator device (Hoke et al., 2014). Heavy-mineral separation was achieved through step-wise magnetic as well as high-density liquid separation techniques, with the final zircon selection carried out under a binocular microscope. Preference was given to intact, prismatic zircons with elongate glass (melt) inclusions parallel to their 'c' axis. U-Pb isotopic analyses by the CA-ID-TIMS technique were carried out following the general procedures described in Ramezani et al. (2011). In order to mitigate the effects of radiation-induced Pb-loss in zircons, the selected zircons were pre-treated by a chemical abrasion method modified after Mattinson (2005) before dissolution. This involved the annealing of zircons at 900 °C for 60 h, followed by leaching in 29 M HF inside high-pressure vessels at 210 °C for 11.5 to 12 h. Thoroughly fluxed and rinsed zircons were spiked with the EARTHTIME ET535 mixed ^{205}Pb-^{233}U-^{235}U tracer (Condon et al., 2015; McLean et al., 2015) and totally dissolved in 29 M HF at 210 °C for 48 h. U and Pb were chemically purified by an HCl-based anion-exchange column procedure and loaded together onto pre-outgassed, zone-refined Re filaments with a silica gel emitter solution. Isotopic measurements were conducted on an Isotopx X62 multi-collector mass spectrometer equipped with a Daly photomultiplier ion-counting system at the Massachusetts Institute of Technology Isotope Laboratory.

Reduction of the mass spectrometric data, calculation of dates, and propagation of uncertainties used the Tripoli and U-Pb_Redux software (Bowring et al., 2011; McLean et al., 2011). Sample dates representing the tuff eruption and deposition ages were calculated based on the weighted mean ^{206}Pb/^{238}U dates derived from coherent clusters of the youngest zircon analyses in each sample, with no younger outliers excluded from age calculation. All uncertainties are reported at the 95% confidence level (2σ) and follow the notation in ± X/Y/Z Ma, where X is the internal (analytical) uncertainty excluding of all external errors, Y incorporates the U-Pb tracer calibration error, and Z includes the latter as well as the decay constant errors of Jaffey et al. (1971). Complete U-Pb data are given in Table 2. Calculated weighted mean dates and their uncertainties are illustrated in the age distribution plots of Fig. 3.

Table 1
Tuff and tuffaceous samples collected for U-Pb geochronology in the Guadalupe Mountains National Park area.

Stratigraphic Position	Sample ID	Locality	GPS	Dates (Ma)
Rader Mbr. (16.5 m above base) (Nicklen et al., 2011)	GM-20	Back Ridge	31°49'28.40"N 104°52'32.10"W	262.58 ± 0.45
Rader Mbr. (Same to GM20)	BR040915-1B	Back Ridge	31°49'28.11"N 104°52'32.95"W	**262.127 ± 0.097**
Pinery Mbr. (middle part)	BCII053117-2	Bear Canyon II	31°54'37.10"N 104°48'46.30"W	–
Pinery Mbr. (stratigraphic position unknown)	NC-17-D-01	Nickel Creek	31°51'41.70"N 104°44'11.40"W	–
Pinery Mbr. (71.1 m above base)	FJ-17-D-93.0 m	Frijole Trail	–	–
Pinery Mbr. (62.2 m above base)	FJ-17-D-84.0 m	Frijole Trail	–	–
Pinery Mbr. (10.1 m above base)	FJ-17-D-31.9 m	Frijole Trail	–	–
Pinery Mbr. (7.4 m above base)	FR060117-1	Frijole Trail	31°54'15.09"N 104°49'12.93"W	**264.23 ± 0.13**
Hegler Mbr. (0.9 m above base)	PHRC-13-D-4	Patterson Hills Roadcut	31°46'39.12"N 104°53'21.61"W	–
Manzanita Mbr. (stratigraphic position unknown)	BCII053117-1	Bear Canyon II	31°54'35.80"N 104°48'45.10"W	–
Manzanita Mbr. (Ramezani and Bowring, 2018)	NippleHill-2	Nipple Hill	31°54'31.91"N 104°47'20.08"W	265.46 ± 0.27
Manzanita Mbr. (1.1 m below top)	PHRC-13-D-3	Patterson Hills Roadcut	31°46'39.12"N 104°53'21.61"W	–
Manzanita Mbr. (2.6 m below top)	PHRC-13-D-2	Patterson Hills Roadcut	31°46'39.12"N 104°53'21.61"W	–
Manzanita Mbr. (5.5 m below top)	PHRC-13-D-1	Patterson Hills Roadcut	31°46'39.12"N 104°53'21.61"W	–
Manzanita Mbr. (stratigraphic position unknown)	GPF-17-D-01	Guadalupe Peak Trail	31°53'47.70"N 104°49'54.40"W	–
South Wells Mbr. (Nicklen et al., 2011)	GM29	Monolith Canyon	31°54'43.99"N 104°46'56.58"W	266.50 ± 0.24
South Wells Mbr. (Basal part)	MC053117-1	Monolith Canyon	31°54'43.50"N 104°46'57.40"W	–
South Wells Mbr. (Basal part)	MC053117-2	Monolith Canyon	31°54'44.38"N 104°46'56.39"W	–
South Wells Mbr. (Basal part)	MC053117-3	Monolith Canyon	31°54'44.37"N 104°46'56.58"W	**266.525 ± 0.078**
Cherry Canyon Formation (2.7 m above base)	GW-13-D-2	Getaway Ledge	31°51'47.54"N 104°47'20.08"W	–
Cherry Canyon Formation (0.9 m above base)	GW-13-D-1	Getaway Ledge	"	–
Getaway Mbr. (stratigraphic position unknown)	JO-17-D-01	Pine Springs	31°53'27.40"N 104°49'04.40"W	–
Pipeline Mbr. (stratigraphic position unknown)	PL060217-1	Guadalupe Pass	31°50'0.04"N 104°50'09.18"W	–

Note: U-Pb dates of this study are shown on bold.
All dates are based on U-Pb CA-ID-TIMS zircon method and reported with analytical uncertainties only.

3.2. Results

3.2.1. MC053117-3

Sample MC053117-3 was collected from a 5 cm-thick greyish-green bentonite near the base of the South Wells Member of the Cherry Canyon Formation exposed at the Monolith Canyon Section (Fig. 2G). All five analyses from this sample with no outliers yielded a weighted mean $^{206}Pb/^{238}U$ date of 266.525 ± 0.078/0.10/0.30 Ma with a mean square of weighted deviates (MSWD) of 0.62. This date is interpreted as the depositional age of the basal South Wells Member.

3.2.2. FR060117-1

Sample FR060117-1 was collected from a 4 cm-thick, buff bentonite in the lower Pinery Member of the Bell Canyon Formation at the Frijole Section (Fig. 2F). Ten grains were analyzed from this sample with the eight youngest forming a coherent cluster yielding a weighted mean $^{206}Pb/^{238}U$ date of 264.23 ± 0.13/0.17/0.33 Ma (MSWD = 0.89) interpreted as the depositional age of the bed FR060117-1. Two slightly older dates are attributed to detrital zircon and excluded from age calculation. This date constrains the Pinery Member near its base.

3.2.3. BR040915-1B

Sample BR040915-1B was collected from a 20 cm-thick bentonite interbedded with the Rader Member limestones at the Back Ridge Section and is thought to be from the same bed as sample GM20 of Nicklen et al. (2015a) collected from 16.5 m above the base of the Rader Member. Three analyzed zircons from this sample, excluding one older (detrital) outlier, form a tight cluster with a weighted mean $^{206}Pb/^{238}U$ date of 262.127 ± 0.097/0.15/0.32 Ma (MSWD = 0.89).

3.3. Bayesian age-stratigraphic model

In this study we use a Bayesian interpolation statistical algorithm to construct an age-stratigraphy model for the Wordian-Capitanian strata at GMNP in order to improve the temporal calibration of the global Capitanian Stage. Our model uses the Bchron software package (Haslett and Parnell, 2008; Parnell et al., 2008) and is essentially similar to that in Shen et al. (2019a). Our new U-Pb date from the Frijole Section along with a previously reported date of 265.46 ± 0.27 Ma from the Nipple Hill Section (Ramezani and Bowring, 2018) and their stratigraphic positions were included in the calculation. The stratigraphic projection of the GSSP horizon onto the Frijole Section based on correlation of the Pinery Member yields an interpolated age of 264.37 + 0.17/−0.18 Ma for the Capitanian base (Fig. 4). Alternatively, the model constrains the bottom and top of the FAD interval of conodont *Jinogondolella postserrata* at the Frijole Section to 263.71 + 0.51/−0.48 Ma and

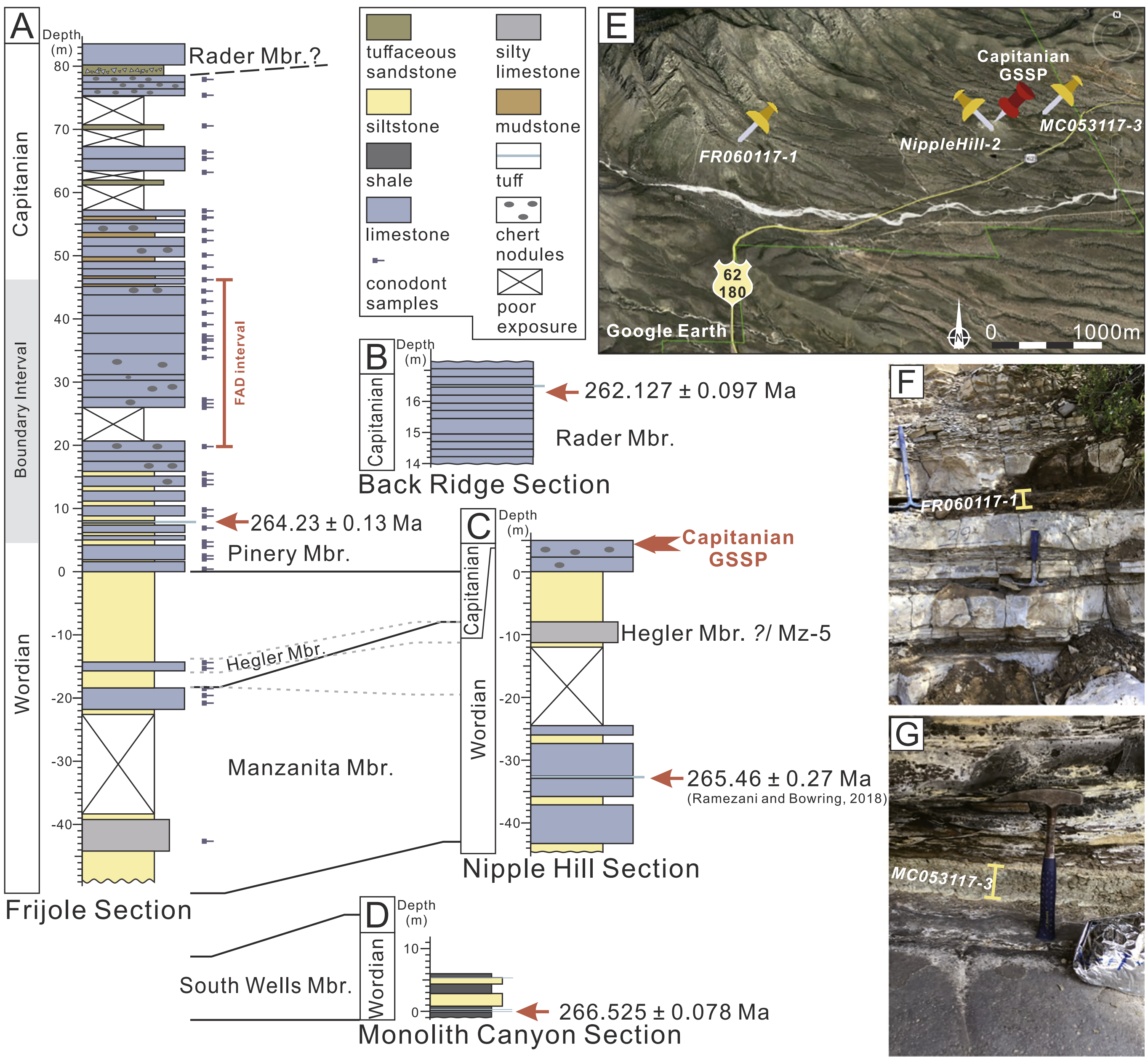

Fig. 2. (A–D) Stratigraphic columns of the Frijole, Back Ridge, Nipple Hill and Monolith Canyon sections marked with the FAD of the conodont *Jinogondolella postserrata* and the U-Pb zircon dates. The date at the Nipple Hill Section is from Ramezani and Bowring (2018). The Frijole Section is marked with the positions of the conodont samples. The grey dashed and black solid lines show the limestone member correlations with and without the Hegler Member present at the Nipple Hill Section, respectively. (E) Locations of the Capitanian GSSP and the geochronology samples around the Nipple Hill area. (F–G) Outcrop photos of the tuffs at the Frijole and Monolith Canyon sections, respectively.

262.6 + 1.6/−2.1 Ma, respectively. All three model ages overlap despite highly variable uncertainties. The weighted average of all three model ages is 264.28 ± 0.16 Ma, which we consider as the best present estimate for the lower Capitanian Stage boundary.

4. Discussion

4.1. Temporal constraints and estimations for the Guadalupian stages

The temporal constraints for the Guadalupian stages have been poor, with only one high-precision U-Pb zircon date available from the type area. This date was first reported by Bowring et al. (1998) at 265.3 ± 0.2 Ma (U-Pb zircon ID-TIMS) from an ash bed about 20 m below the Capitanian GSSP at Nipple Hill in GMNP. Recently, Ramezani and Bowring (2018) applied the chemical abrasion (CA) pretreatment technique and the EARTHTIME U-Pb tracer to zircon analyses from the same ash bed (NippleHill-2), and revised the date to 265.46 ± 0.27 Ma (Fig. 3). Although this date itself is precise, the stratigraphic position of the bed has been the subject of debate. The bed was initially reported as lying 20 m below the Capitanian GSSP between the Hegler Member and the Pinery Member (Bowring et al., 1998), but was revised to 37.2 m below the Capitanian boundary and 2 m above the Manzanita Member of the Cherry Canyon Formation at the Nipple Hill Section (Glenister et al., 1999). Nicklen et al. (2015b) reported two ash beds near 37.2 m below the Capitanian GSSP at the Nipple Hill Section and correlated this interval to the Manzanita Member based on the geochemical characteristics of the phenocrysts in the bentonites. The date of 265.46 ± 0.27 Ma was thus from the Manzanita Member at the Nipple

Table 2
U-Pb isotopic data for CA-ID-TIMS zircon analyses from the tuffs in Guadalupe Mountains National park, Texas.

Sample					Ratios								Ages (Ma)						
Fractions	Pb(c) (pg)	Pb*/Pb(c)	U (pg)	Th/U	^{206}Pb/^{204}Pb	^{208}Pb/^{206}Pb	^{206}Pb/^{238}U [f]		^{207}Pb/^{235}U [f]		^{207}Pb/^{206}Pb [f]		^{206}Pb/^{238}U	err (2σ)	^{207}Pb/^{235}U	err (2σ)	^{207}Pb/^{206}Pb	err (2σ)	corr.
[a]	[b]	[b]	[c]		[d]	[e]	ratio	err (2σ%)	ratio	err (2σ%)	ratio	err (2σ%)							coef.
Back Ridge Section																			
BR040915-1B: Rader Member																			
z1	0.20	41.9	175	0.89	2275.3	0.281	0.041484	(.08)	0.29530	(.58)	0.05165	(.55)	**262.03**	**0.20**	262.7	1.3	269	13	0.39
z2	0.16	89.1	290	1.15	4539.0	0.364	0.041500	(.07)	0.29540	(.32)	0.05165	(.30)	**262.12**	**0.17**	262.80	0.75	268.8	7.0	0.36
z3	0.17	121.6	394	1.27	6021.0	0.402	0.041511	(.06)	0.29502	(.29)	0.05157	(.26)	**262.19**	**0.15**	262.50	0.66	265.3	6.1	0.42
z5	1.37	10.7	281	1.27	548.1	0.403	0.041655	(.19)	0.29948	(2.16)	0.05217	(2.10)	263.08	0.49	266.0	5.1	292	48	0.34
Frijole Section																			
FR060117-1: Pinery Member																			
z1	1.41	7.7	255	0.44	485.0	0.138	0.041830	(.22)	0.30036	(2.47)	0.05210	(2.41)	**264.17**	**0.56**	266.7	5.8	289	55	0.33
z2	0.32	16.0	119	0.46	981.0	0.145	0.041968	(.12)	0.29854	(1.24)	0.05162	(1.21)	**265.02**	**0.32**	265.3	2.9	267	28	0.33
z3	0.20	18.6	84	0.45	1136.9	0.142	0.041883	(.11)	0.30043	(1.05)	0.05205	(1.02)	**264.49**	**0.28**	266.7	2.5	286	23	0.32
z4	0.27	27.5	172	0.42	1686.7	0.131	0.041829	(.08)	0.29856	(.71)	0.05179	(.69)	**264.16**	**0.21**	265.3	1.7	275	16	0.35
z5	0.33	12.8	100	0.42	797.7	0.133	0.041803	(.19)	0.29672	(1.66)	0.05150	(1.61)	**264.00**	**0.48**	263.8	3.9	262	37	0.34
z7	0.45	11.2	116	0.46	693.6	0.144	0.041852	(.16)	0.29825	(1.77)	0.05171	(1.72)	**264.30**	**0.42**	265.0	4.1	272	39	0.32
z8	0.31	3.9	28	0.49	247.8	0.154	0.041965	(.45)	0.30145	(5.39)	0.05212	(5.24)	265.0	1.2	268	13	290	120	0.38
z9	0.39	4.2	39	0.39	274.8	0.124	0.041820	(.49)	0.29918	(4.78)	0.05191	(4.63)	**264.1**	**1.3**	266	11	280	106	0.36
z10	0.36	12.3	103	0.47	755.9	0.148	0.041807	(.17)	0.29930	(1.63)	0.05195	(1.59)	**264.03**	**0.43**	265.9	3.8	282	36	0.31
z12	0.37	9.9	88	0.40	625.0	0.125	0.041855	(.22)	0.30043	(2.09)	0.05208	(2.01)	264.32	0.57	266.7	4.9	288	46	0.39
Monolith Canyon Section																			
MC053117-3: South Wells Member																			
z6	0.27	68.6	393	0.76	3830.5	0.240	0.042239	(.10)	0.30028	(.43)	0.05158	(.42)	**266.70**	**0.26**	266.6	1.0	266.0	9.6	0.21
z7	0.26	65.4	357	0.74	3670.3	0.234	0.042208	(.04)	0.30066	(.34)	0.05169	(.33)	**266.51**	**0.12**	266.92	0.81	270.5	7.7	0.28
z8	0.33	31.8	233	0.64	1842.4	0.201	0.042218	(.08)	0.30123	(.70)	0.05177	(.68)	**266.57**	**0.22**	267.4	1.6	274	16	0.34
z9	0.39	23.9	195	0.80	1333.2	0.254	0.042212	(.11)	0.30127	(.97)	0.05179	(.94)	**266.53**	**0.28**	267.4	2.3	275	22	0.35
z10	0.26	42.7	233	0.81	2367.6	0.254	0.042203	(.06)	0.29988	(.52)	0.05156	(.50)	**266.47**	**0.15**	266.3	1.2	265	12	0.32

Notes:
Mass fractionation correction of 0.25%/amu ± 0.04%/amu (atomic mass unit) was applied to single-collector Daly analyses, where single Pb tracer was used.
All common Pb assumed to be laboratory blank. Total procedural blank less than 0.1 pg for U.
Blank isotopic composition: ^{206}Pb/^{204}Pb = 18.15 ± 0.47, ^{207}Pb/^{204}Pb = 15.30 ± 0.30, ^{208}Pb/^{204}Pb = 37.11 ± 0.87.
Corr. coef. = correlation coefficient.
Ages calculated using the decay constants λ_{238} = 1.55125E-10 y^{-1} and λ_{235} = 9.8485E-10 y^{-1} (Jaffey et al. 1971).
[a] Thermally annealed and pre-treated single zircon. Data used in age calculations are in bold.
[b] Total common-Pb in analyses. Pb* is radiogenic Pb content.
[c] Total sample U content.
[d] Measured ratio corrected for spike and fractionation only.
[e] Radiogenic Pb ratio.
[f] Corrected for fractionation, spike and blank. Also corrected for initial Th/U disequilibrium using radiogenic ^{208}Pb and Th/U$_{magma}$ = 2.8.

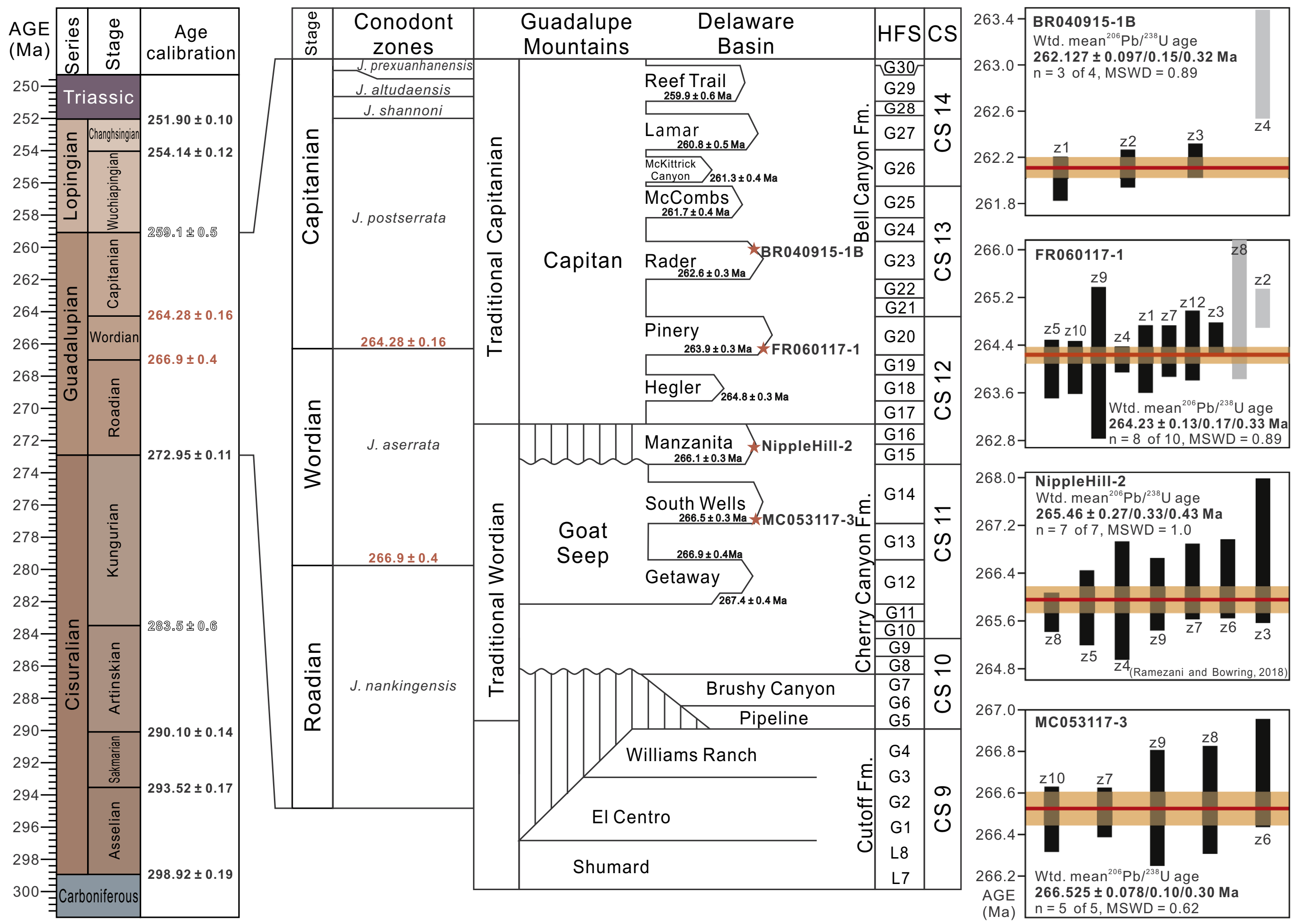

Fig. 3. Summary of the conodont biostratigraphy, lithostratigraphy, and chronostratigraphy of the Guadalupian in West Texas. The lithostratigraphy and conodont zones are modified after Wardlaw and Nestell (2010) and Shen et al. (2019b). Diagrams on the right show the dates constraining the limestone members in GMNP. The vertical bars show the $^{206}Pb/^{238}U$ dates of individual zicron grains with 2σ error hights. Zircon analyses involved in calculation are in balck. Horizontal lines are calculated sample dates with the width of the shaded band representing internal uncertainty in the weighted mean date at 95% confdence level. The Nipple Hill Manzanita Member date is from Ramezani and Bowring (2018). The sequence stratigraphic framework is modified after Frost et al. (2012) and Kerans et al. (2014). The bases of the limestone members of the Cherry Canyon and Bell Canyon formations are marked with the ages estimated based on temporal constraints on the HFSs.

Hill Section. Accordingly, the base of the Capitanian was inferred to be younger than the age of 265.46 ± 0.27 Ma in Ramezani and Bowring (2018), but without an upper stratigraphic age constraint to allow an objective and quantitative age interpolation.

Forty-two conodont samples were collected for constraining the first occurrence (FO) of *Jinogondolella postserrata* at the Frijole Section (Fig. 2A). The new conodont biostratigraphic data at the Frijole Section suggested that the FAD of the conodont *J. postserrata* occurs 12.4 m to 38.8 m above the ash bed FR060117-1 (Yuan et al., pers. comm.). The uncertainty in the exact position of the FAD of *J. postserrata* at the Frijole Section is due to the low conodont abundance in this interval. In addition, the Capitanian conodont samples at the Nipple Hill Section contain abundant *Jinogondolella aserrata* with few *J. postserrata*, which raises another potential issue for recognizing the exact position of the lower boundary of the Capitanian Stage in the conodont-rare interval at the Frijole section. The FAD of *J. postserrata* at the Frijole Section is stratigraphically higher than that at the Nipple Hill Section based on lithostratigraphic correlation of the base of the Pinery Member. One possible explanation is that the lower Bell Canyon Formation might be more condensed at the Nipple Hill Section. The thickness of the Pinery Member in the southeastern Guadalupe Mountains area varies from about 80 m along the slope of the basin to less than 15 m towards the basin center (King, 1948). Thus, the Pinery Member might be thinner at the Nipple Hill Section than at the Frijole Section. Besides, the interval between the top of the Manzanita Member and the base of the Pinery Member at the Frijole Section is nearly 20 m, while that at the Nipple Hill Section is merely 8 m, if the Hegler Member is considered absent from the latter. Thus, the FAD of *J. postserrata* could conceivably shift from below the ash bed FR060117-1 to above it. The Bchron age-depth model yields an age of 263.71 + 0.51/−0.48 Ma for the base of the FAD interval of the conodont *J. postserrata*, and 262.6 + 1.6/−2.1 Ma for the top of the FAD interval of *J. postserrata* at the Frijole Section. The two model ages constraining the FAD interval at the Frijole Section overlap with the age of 264.37 + 0.17/−0.18 Ma based on the conodont data at the Nipple Hill Section (projected onto the Frijole Section) considering their large uncertainties. Although further detailed work is needed to establish a robust correlation of conodont biostratigraphy between the two sections, the weighted average of the above three model ages at 264.28 ± 0.16 Ma is considered as the best current estimate for the lower Capitanian Stage boundary.

A new U-Pb zircon date of 266.525 ± 0.078 Ma was obtained from the basal part of the South Wells Member in the Monolith Canyon Section. Nicklen (2011) also reported a bentonite from the base of the South Wells Member which was dated at 266.50 ± 0.24 Ma (n = 8, MSWD = 1.5) by the CA-ID-TIMS method following the same U-Pb analytical procedures and protocols as those of this study. This sample

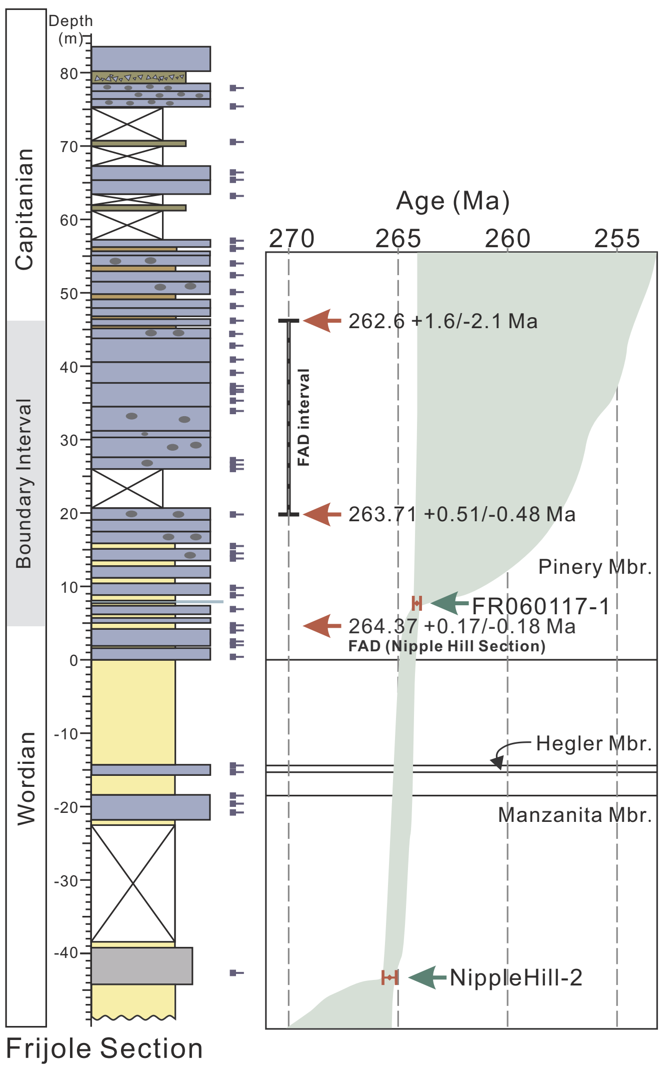

Fig. 4. Bchron age-depth model with 95% confidence level uncertainty for the composite Nipple Hill-Frijole sections marked with the interpolated ages for the possible FADs of *Jinogondolella postserrata*. The grey interval between Wordian and Capitanian suggests that the precise boundary at the Frijole Section is still not fixed based on the current available conodonts.

was collected close to sample MC053117-3 in the Monolith Canyon drainage based on the GPS coordinates of the two samples, and its date is indistinguishable with that of MC053117-3 within uncertainty. Our new date from the South Wells Member provides a minimum age constraint for the Wordian-base boundary.

Nicklen (2011) reported another ash bed from the Rader Member of the Bell Canyon Formation at the Back Ridge Section, which was dated at 262.58 ± 0.45 Ma (n = 4, MSWD = 2.0) by the CA-ID-TIMS method. Our BR040915-1B sample is from the same outcrop with a weighted mean $^{206}Pb/^{238}U$ date of 262.127 ± 0.097 Ma. This date is more precise and overlaps with that of Nicklen (2011) within uncertainty, placing a minimum age bracket on the base Capitanian boundary. However, the stratigraphic projection of the ash bed BR040915-1B onto the Frijole Section is difficult due to poor exposure in the upper part of the section (Fig. 2A), making it impractical to utilize this date in our Wordian-Capitanian chronostratigraphic model. A U-Pb zircon date of 260.57 ± 0.065/0.14/0.31 Ma (MSWD = 1.8, n = 5) by the CA-ID-TIMS method was reported from the top of the Meade Peak Member of the upper Phosphoria Formation in Idaho (Davydov et al., 2018a). However, the conodont fossils recovered from this interval are insufficient to allow a reliable correlation to the Capitanian type area.

Few radioisotopic ages are available from the Roadian. No ash beds have been discovered from the basal Roadian in the type area in GMNP, West Texas, while a few zircon U-Pb dates by the CA-ID-TIMS method have been reported from the Boreal and Tethyan regions. Davydov et al. (2018b) reported a high-precision U-Pb zircon date of 274.0 ± 0.12 Ma from an ash bed immediately above sediments yielding the ammonoid *Sverdrupites harkeri* in the Russian Far East (Kutygin and Biakov, 2015). Since both the conodont *J. nankingensis* and the ammonoid *S. harkeri* were found in the Assistance Formation in Arctic Canada (Leven and Bogoslovskaya, 2006), Davydov et al. (2018b) proposed that the base of the Roadian was older than 274.0 ± 0.12 Ma and might be as old as *ca.* 277 Ma. However, no conodonts have been found associated with the *S. harkeri* ammonoid horizon in Russian Far East, and the ammonoid *Sverdrupites* has not been reported in the type Roadian (or Guadalupian) area in West Texas. Additionally, further work is needed to establish whether the FAD of *J. nankingensis* in the Boreal provinces is synchronous with that in West Texas (Shen et al., 2019b). A CA-ID-TIMS zircon U-Pb date of 272.95 ± 0.11 Ma has been reported from the base of the Kuhfeng Formation in Chaohu of southeastern China, constraining the FAD of the conodont *J. nankingensis* and thus the Cisuralian-Guadalupian boundary age in South China (Wu et al., 2017). The Guadalupian conodont zones in South China show strong correlation with those in West Texas, but the synchronicity of the FAD of *J. nankingensis* in the two regions separated by the Panthalassic ocean remains to be confirmed (Henderson and Mei, 2003; Leven and Bogoslovskaya, 2006; Henderson, 2018; Shen et al., 2019b). Until further geochronology from North America tests the transcontinental correlation of the Guadalupian, the date of 272.95 ± 0.11 Ma serves as the best age constraint for the base of the Guadalupian.

Our new geochronology also provides a temporal framework for the high-frequency sequences of the Cherry Canyon and Bell Canyon formations in the southern Guadalupe Mountains area. A total of 17 high-frequency sequences (HFSs) grouped into four composite sequences (CS) were recognized from the Getaway Member to the Reef Trail Member in GMNP (Frost et al., 2012; Kerans et al., 2014; Fig. 3). Our Rader ash age of 262.127 ± 0.097 Ma has been correlated to the top of HFS G23 (Nicklen et al., 2015a), whereas our Monolith Canyon ash age of 266.525 ± 0.078 Ma correlates with the base of the HFS G14 (Kerans et al., 2014). Thus, the interval from the basal South Wells Member to the middle Rader Member encompassing ten HFSs was deposited over a *ca.* 4.4 myr time span, giving each HFS an average duration of *ca.* 0.44 myr. Accordingly, the onset of the South Wells Member can be estimated at 266.5 ± 0.3 Ma, the Manzanita Member at 266.1 ± 0.3 Ma, the Hegler Member at 264.8 ± 0.3 Ma, the Pinery Member at 263.9 ± 0.3 Ma and the Rader Member at 262.6 ± 0.3 Ma (Fig. 3). These estimates for the bases of the limestone members are consistent with direct U-Pb dates from each unit within uncertainty (Fig. 3). Assuming that the HFSs continued above the Rader Member in the same manner, the base of the Reef Trail Member would be estimated at 259.9 ± 0.6 Ma (Fig. 3). The topmost part of the Reef Trail Member is estimated to 259.5 ± 0.7 Ma. This would place the GLB in the overlying evaporitic Castile Formation where no conodonts are found (Zhong et al., 2014; Ramezani and Bowring, 2018; Shen et al., 2019b). This is consistent with the new conodont biostratigraphy from the area, which documents the topmost conodont zone as *J. prexuanhanensis* instead of *Clarkina postbitteri hongshuiensis* (Lambert et al., 2010; Wardlaw and Nestell, 2010; Shen et al., 2019b). A severe regression starting from the *J. prexuanhanensis* Zone could be reflected by the evaporitic Castile Formation of GMNP, because a regression has also been recorded in the same conodont zone in sections in South China (Mei et al., 1999a, 1999b; Wignall et al., 2009b). If the cyclic pattern of the HFSs is also projected downward to the Getaway Member, we infer that the base of the Getaway Member would be 267.4 ± 0.4 Ma. The base of the Wordian Stage is in the top of the Getaway Member, and thus could be estimated at 266.9 ± 0.4 Ma (Fig. 3; Glenister et al., 1999).

Five high-precision U-Pb CA-ID-TIMS zircon dates upward from the early Midian stage were recently reported from southwestern Japan (265.76 ± 0.03 Ma to 267.46 ± 0.04 Ma; Davydov and Schmitz, 2019). As the base of the Midian stage in the Tethyan region is assigned to the middle Wordian (Lucas and Shen, 2018; Zhang and Wang, 2018), the oldest Midian date suggests that the base of the Wordian is older than 267.46 ± 0.04 Ma, which is inconsistent with our estimates. However, the lower boundary of the Midian stage in Japan is ambiguous (Davydov and Schmitz, 2019), and correlations from the sections in Japan to West Texas are uncertain because of strong faunal provincialism and a lack of additional correlation criteria (*e.g.*, geochemistry or paleomagnetism). The two younger dates from the Midian of Japan are biostratigraphically constrained by fusulinids, whereas the older three are interbedded with siliciclastic rocks lacking marine fossils, and are thus of uncertain stratigraphic position (Davydov and Schmitz, 2019). Further direct high-precision geochronology for the Wordian in West Texas could improve correlations to the Tethyan regions.

4.2. Implications for the end-Guadalupian extinction

The geochronology presented here provides the best temporal constraints on the Capitanian and Wordian stages in West Texas. The lower Capitanian boundary age is estimated at 264.28 ± 0.16 Ma by the Bayesian age-stratigraphic modeling, or 0.94 ± 0.38 myr younger than the estimate from Ramezani and Bowring (2018). The new estimated lower Wordian boundary age is 266.9 ± 0.4 Ma, or 1.9 ± 0.6 myr younger than the age in the International Chronostratigraphic Chart (ICC) (Henderson et al., 2012; Cohen et al., 2013). These new estimates also change our estimates for the duration of the three stages. To be specific, our data shorten the estimated duration of the Capitanian from 6.12 ± 0.60 myr in the ICC to 5.18 ± 0.52 myr (Henderson et al., 2012). The new duration of the Wordian is 2.6 ± 0.4 myr, which is 1.0 ± 0.7 myr shorter than previously estimated (Henderson et al., 2012). As the lower boundary of the Wordian is younger, the duration of the Roadian increases from 4.15 ± 0.51 myr to 6.0 ± 0.4 myr. These changes in the estimated stage durations have significant effects on assessing the rates of the geological and biological events, such as the end-Guadalupian mass extinction. Since it was first recognized by Jin et al. (1994) and Stanley and Yang (1994), the existence, timing and possible mechanisms of the end-Guadalupian biotic crisis have been debated. The extinction and origination rates during the Guadalupian have been reported by several studies, especially during the Capitanian which is the key period of this extinction event (Shen and Shi, 2002, 2009; Clapham et al., 2009; Groves and Wang, 2013; Day et al., 2018). The Capitanian duration in this study is up to *ca.* 1.6 myr shorter than those applied in the above studies, which consequently increases extinction/origination rates by up to 23%, and thus changes assessments of the extinction event.

Whether a Guadalupian mass extinction occurred during the middle Capitanian (Bond et al., 2010a, 2010b) or the late Capitanian (Shen and Shi, 2009; Groves and Wang, 2013; Day et al., 2015) remains contentious. Our new temporal estimations for the limestone members in West Texas provide some temporal constraints for the end-Guadalupian extinction event. The Capitanian conodont zones in South China show strong correlation with those in West Texas, and the complete Capitanian conodont lineage can be recognized in South China (Jin et al., 2006). The *Jinogondolella postserrata*, *J. shannoni*, *J. altudaensis* and *Clarkina postbitteri hongshuiensis* conodont zones, in ascending order, were reported from the Capitanian in West Texas (Lambert et al., 2002, 2010; Wardlaw and Nestell, 2010). However, new conodont biostratigraphic interpretations suggest that the Capitanian in West Texas is instead composed of the zones of *J. postserrata*, *J. shannoni*, *J. altudaensis* and *J. prexuanhanensis* in ascending order, with the younger conodont zones, including *J. xuanhanensis*, *J. granti* and *C. postbitteri hongshuiensis*, missing, probably represented by the time of deposition of the Castile Formation in the Delaware Basin (Shen et al., 2019b).

The turnover or extinction of different fossil groups occurred at different stratigraphic levels, as summarized by Shen and Shi (2009) and Chen and Shen (2019). The rugose corals disappeared below the *J. altudaensis* Zone (Wang and Sugiyama, 2000, 2001), followed by a decrease of the brachiopods in the *J. xuanhanensis* Zone (Shen and Shi, 2009; Shen et al., 2009), and the fusulines together with the collapse of reefs in the *J. granti* Zone (Jin et al., 2006; Wignall et al., 2009b; Groves and Wang, 2013; Zhang and Wang, 2018; Huang et al., 2019a). Conodonts experienced rapid turnover immediately below the GLB from the typical Guadalupian *Jinogondolella* assemblage to the Lopingian *Clarkina* assemblage (Mei et al., 1998; Jin et al., 2006; Shen and Shi, 2009). Some evidence suggests the biotic crisis may have persisted to the earliest Wuchiapingian: *Kufengoceras*, a typical Guadalupian ammonoid in the Paleo-Tethys region, persisted into the earliest Wuchiapingian conodont zone of *C. postbitteri postbitteri*, and subsequent Lopingian ammonoids likely became abundant and highly diverse from the *C. liangshanensis*-*C. orientalis* zones at the Penglaitan Section in South China (Ehiro and Shen, 2008; Chen and Shen, 2019). Although the data discussed were from a straight reading of the fossil record without confidence interval analysis, they can still provide information for the general extinction interval. In summary, this biotic crisis began in the *J. altudaensis* Zone and continued to the end of the Capitanian or possibly into the earliest Wuchiapingian.

Bond et al. (2010a) suggested that the onset of the end-Guadalupian mass extinction was from the *J. altudaensis* to *J. prexuanhanensis* zones (up to five conodont zones below the top of the Capitanian) in South China, and hence they considered the extinction to have occurred in the middle Capitanian. However, based on our temporal estimation for the limestone members in the Delaware Basin, conodonts experienced a rapid rate of evolution during the extinction interval. The *J. postserrata* and *J. shannoni* conodont zones extend from the lower part of the Pinery Member to the base of the Reef Trail Member – *ca.* 4.4 myr based on our estimates, while the remaining five Capitanian conodont zones span approximately the last 0.8 myr of the Capitanian. The estimated total duration of those conodont zones from *J. altudaensis* to *C. postbitteri hongshuiensis* is much shorter than previously recognized (*e.g.* Sun et al., 2010). The increased rate of evolution for conodonts is coincident with the overall extinction interval summarized above. One possible explanation for the more rapid evolution is that the Guadalupian genus *Jinogondolella* may have suffered stressful conditions before being replaced by the Lopingian genus *Clarkina*.

The conodont zone of *J. altudaensis* starts from the base of the Reef Trail Member in West Texas (Lambert et al., 2010; Wardlaw and Nestell, 2010), constraining the onset of the extinction to 259.9 ± 0.6 Ma based on our estimates (Figs. 3 and 5). Day et al. (2015) reported a zircon date of 260.259 ± 0.081 Ma (CA-ID-TIMS) in the terrestrial tetrapod extinction interval in South Africa, which is roughly consistent with our temporal estimates for the marine extinction interval. The terrestrial plant extinction was recognized in the same horizon in the end of the Guadalupian in South Africa (Retallack et al., 2006). Thus, the marine and nonmarine extinctions might be synchronous near the end of the Guadalupian (Lucas, 2017). Previous disagreements over the timing of the extinction may have been largely caused by failure to realize the varying duration of Capitanian conodont zones. Despite the apparent variation in the onset of extinction in different fossil groups based on the high-resolution conodont biostratigraphy, the entire biotic crisis may have been quite brief.

A causal relationship between the ELIP and the end-Guadalupian extinction has long been proposed (Zhou et al., 2002; He et al., 2007; Wignall et al., 2009a; Sun et al., 2010; Chen and Shen, 2019; Chen and Xu, 2019; Huang et al., 2019a), but the precise and accurate emplacement history of the ELIP has not been resolved, which makes evaluating the hypothesis difficult. Several radioisotopic dates associated with the ELIP have been reported (Shellnutt et al., 2012 and references therein; Xu et al., 2013; Zhong et al., 2013, 2014; Huang et al., 2016; Li

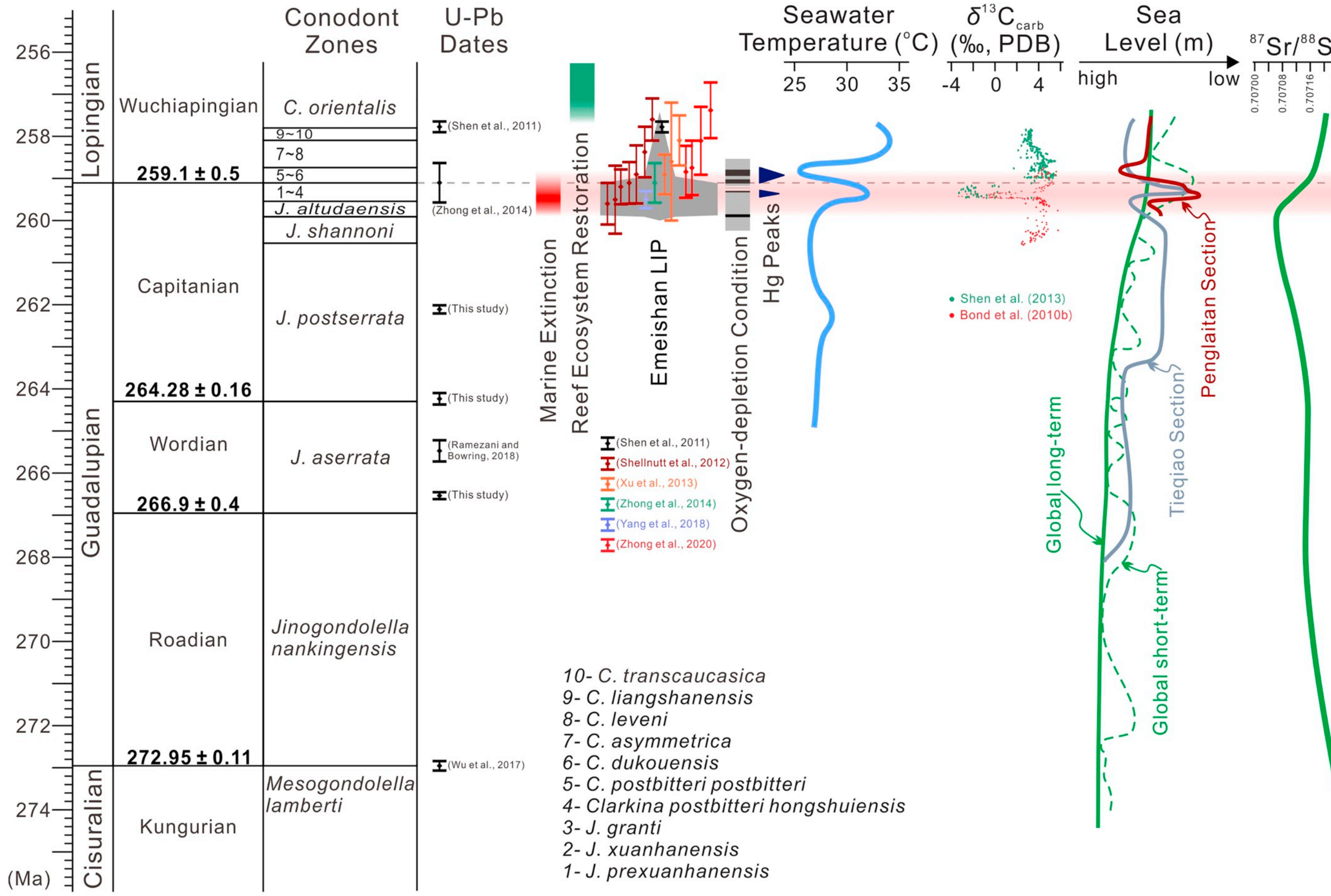

Fig. 5. Summary of the end-Guadalupian extinction and the accompanying major geological events. The ages for the bases of the Wuchiapingian and Rodian are from Zhong et al. (2014) and Wu et al. (2017), respectively. The ages of the basal Capitanian and Wordian are based on the calculation in this study. The Guadalupian and early Wuchiapingian conodont zones are from Jin et al. (2006). The temporal distribution of the conodont zones in the early Wuchiapingian is extracted from Yuan et al. (2019), while that in the Guadalupian is based on the estimation in this study. The restoration of the reef ecosystem is modified from Huang et al. (2019b). The CA-ID-TIMS zircon U-Pb dates associated with the ELIP are from Shen et al. (2011), Shellnutt et al. (2012), Xu et al. (2013), Zhong et al. (2014, 2020) and Yang et al. (2018). The $\delta^{13}C_{carb}$ trends are modified after Bond et al. (2010b) and Shen et al. (2013). The relative seawater temperature fluctuations are from Chen et al. (2011). The marine strontium isotope curve is from Wang et al. (2018). The global and regional sea-level changes are modified after Haq and Schutter (2008) and Mei et al. (1999a, 1999b), respectively.

et al., 2018; Yang et al., 2018). Most of the ages were zircon U-Pb dates by the microbeam analyses with errors of up to 4% (Klötzli et al., 2009; Schmitz and Kuiper, 2013), or ^{40}Ar-^{39}Ar dates with the danger of partial resetting (*e.g.* Boven et al., 2002; Lo et al., 2002). Although those dates cluster around 260 Ma, individual samples have errors greater than 2 myr, which might be longer than the total duration of the ELIP. Hence these dates are too imprecise to evaluate the temporal relationship between the ELIP and the end-Guadalupian extinction. Recently, U-Pb zircon dates by the CA-ID-TIMS method from samples associated with the ELIP were reported (Fig. 5; Shen et al., 2011; Shellnutt et al., 2012; Zhong et al., 2014, 2020; Yang et al., 2018). Dates for intrusive rocks of the ELIP ranging from 259.69 ± 0.72 Ma to 257.6 ± 0.5 Ma constrained the emplacement of the ELIP between *ca.* 260 Ma to 257 Ma (Shellnutt et al., 2012). The date of the felsic ignimbrite in the topmost of the ELIP basalt at the Binchuan Section constrained the termination of the ELIP basalt to 259.1 ± 0.5 Ma (Zhong et al., 2014). Yang et al. (2018) reported a consistent date (259.51 ± 0.21 Ma) from the top of the ELIP basalt at the Pu'an Section. The date of 257.79 ± 0.14 Ma of the tuff associated with the ELIP at the Shangsi Section indicated that the ELIP may have continued to *ca.* 257.8 Ma (Shen et al., 2011; Huang et al., 2018). The new dates ranging from 258.82 ± 0.61 Ma to 257.39 ± 0.68 Ma of the ash beds from the extrusive alkaline felsic magmatism of the ELIP constrained its waning stage to *ca.* 257.4 Ma (Zhong et al., 2020). In addition, there are three unpublished CA-ID-TIMS zircon dates from the acidic rocks in the top of the Emeishan basalt (258.9 ± 0.5 Ma) and the ash beds close to the GLB in Guizhou and Sichuan area (258.1 ± 0.6 Ma and 258.6 ± 1.4 Ma) (Xu et al., 2013). Accordingly, the peak eruptive pulse of the ELIP may have been from *ca.* 260 Ma to 259 Ma, followed by the waning stage continuing to *ca.* 257.4 Ma (Fig. 5).

The limestone and the overlying Emeishan Basalt contacts were dated by high-resolution conodont biostratigraphy in South China, suggesting that the ELIP started to erupt during the *J. altudaensis* Zone and greatly increased in extent and volume in the *J. xuanhanensis* Zone (Sun et al., 2010). The mercury concentration/total organic carbon (Hg/TOC) ratios suggested that the ELIP may have continued to the *C. dukouensis* Zone in the early Wuchiapingian (Huang et al., 2019a). Drowning events around the GLB have been interpreted as reflecting the eruptive phases of ELIP continuing to the *C. transcaucasica* Zone (Bagherpour et al., 2018a, 2018b). Therefore, the emplacement of ELIP may have extended from *ca.* 260 Ma (*J. altudaensis* Zone) to *ca.* 257.8 Ma (*C. transcaucasica* Zone) based on the conodont age estimation and calculation (Yuan et al., 2019), which is coincident with the ELIP age based on the CA-ID-TIMS zircon U-Pb dates.

Thus, the end-Guadalupian extinction is coincident with the peak eruptive pulse of ELIP but may have ended before the cessation of the

ELIP, supporting suggestions that the onset of ELIP may have contributed to the end-Guadalupian extinction. The last phases of the ELIP in the early Wuchiapingian may have caused further ecosystem stress. Reef ecosystems did not recover in South China until the middle-late Wuchiapingian conodont zone of *Clarkina orientalis* (Huang et al., 2019b). The base of the conodont *C. orientalis* Zone was calculated as 257.81 ± 0.14 Ma based on the Shangsi Section (Shen et al., 2011; Yuan et al., 2019). If the return of reef ecosystems is a reliable marker of general recovery, this age is coincident with the end of the ELIP based on the radioisotopic dates by Zhong et al. (2020), indicating that the ELIP may have hampered ecosystem restoration after the end-Guadalupian extinction (Huang et al., 2019b).

It is important to notice that the interval of the end-Guadalupian extinction is shorter than that of the ELIP. Although the longer duration of the ELIP might be partly due to the lack of high-precision temporal constraints, several lines of evidence, *e.g.*, the drowning events reported by Bagherpour et al. (2018a, 2018b) and the Hg peaks by Huang et al. (2019a), still indicate the ELIP eruptive activities after the extinction in the early Wuchiapingian. Besides, the CA-ID-TIMS zircon U-Pb dates on the waning stage of the ELIP in Zhong et al. (2020) also indicate that the duration of the ELIP is longer than that of the end-Guadalupian extinction. Therefore, the peak phase of the ELIP might play a more critical role than its total emplacement in the biotic crisis and environmental changes. Otherwise, the ELIP is not the only contributor to the extinction. The largest global and regional regression during the Paleozoic (Mei et al., 1999a, 1999b; Haq and Schutter, 2008) may have contributed to the biotic crisis by reducing shallow-water marine habitats and leading to no deposition or evaporation in the terrestrial system (Jablonski, 1985; Shen and Shi, 2002). Other significant global geological events have been documented during this key period (Fig. 5). A major negative, global carbon isotope excursion in the *J. prexuanhanensis* to *J. xuanhanensis* zones of the late Capitanian has been attributed to a large carbon cycle disturbance during the end-Guadalupian extinction event (Bond et al., 2010b; Shen et al., 2013; Jost et al., 2014; Cao et al., 2018). However, the negative excursion has not been observed from all sections across the GLB (*e.g.* Chen et al., 2011; Liu et al., 2013; Jost et al., 2014), because carbon isotopic compositions may have been disturbed by local burial conditions or diagenetic effects. Fluctuations in the carbon cycle at this time do not appear to have been as severe as those associated with the end-Permian extinction (Shen et al., 2011). Seawater temperature reconstructed from $\delta^{18}O$ of the gondollelid conodont in South China experienced about 4 °C warming during the latest Guadalupian, followed by a 6–8 °C cooling across the GLB and into the earliest Wuchiapingian, and again significant warming around the *C. asymmetrica* Zone and cooling from the *C. leveni* Zone (Chen et al., 2011, 2013; Yang et al., 2018). It is interesting that the sea-level eustasy was coincident with the seawater temperature fluctuations reconstructed from the gondollelids. Chen et al. (2011) suggested that variations of the oxygen isotopes in the gondollelid conodonts might be controlled by both the seawater depths they lived in and the paleoclimatic changes. Specifically, the gondollelids probably lived in the relatively deep waters during the transgression and thus recorded lower temperatures, while they had to survive in the shallower waters during the regression and thus recorded higher temperatures. The warming interval during the latest Capitanian may have been attributed to the emplacement of the ELIP and the severe regression. The cooling events during the Wuchiapingian may have been associated with ELIP basaltic weathering, which may have consumed atmospheric pCO_2 (Yang et al., 2018). The therapsid tooth apatite oxygen isotope in South Africa also indicated a cooling interval during the early Wuchiapingian, but no warming interval in the earliest Wuchiapingian was recorded (Rey et al., 2016). It might be attributed to the sparse data that missed the warming interval. Otherwise, the warming interval recorded by the gondollelid conodonts in South China could actually indicate a rapid regressive event. Seawater strontium isotopes dropped to a minimum during the middle-late Capitanian (Wang et al., 2018). The long-term oxygen-depletion conditions (Saitoh et al., 2013; Wei et al., 2016; Smith et al., 2020) and the widespread shoaling of sulfidic waters (Zhang et al., 2015) in the late Capitanian may have contributed to the end-Guadalupian extinction as well. These complex geological events induced dramatic environmental changes during the extinction interval.

4.3. Correlation of the Illawarra Reversal

The Illawarra Reversal (IR) marks the first normal magnetozone after the long-term dominance of reverse polarity from the Late Carboniferous to the middle Guadalupian (Kiaman Superchron). The magnetostratigraphy above the IR from the middle Permian to the Triassic is dominated by frequent alternations of normal and reverse polarity intervals (Illawarra Superchron) (Isozaki, 2009; Hounslow and Balabanov, 2018). The IR can serve as a global correlation maker for Guadalupian successions that lack appropriate index fossils or direct radioisotopic dates, but its age has not been resolved yet (Hounslow and Balabanov, 2018; Lucas and Shen, 2018). The IR was first proposed in the Sydney Basin, southeastern Australia (Irving and Parry, 1963). This geomagnetic polarity reversal event has been recognized elsewhere (*e.g.*, Russia, America, North China, Japan, Germany, South Africa) (Hounslow and Balabanov, 2018 and references therein). In West Texas, the magnetic carriers in the stratotype successions have been oil-saturated, which made them unlikely to yield good paleomagnetic data. Much of the backreef strata have yielded paleomagnetic polarities, despite that no detailed data have been published and thus the reliability of those data are unknown (Steiner, 2006). Steiner (2006) positioned the IR in the backreef middle Grayburg Formation or the lowermost part of the overlying Queen Formation. Kerans et al. (2014) correlated this interval to the HFSs of G12-G13 in the latest Roadian to earliest Wordian, and thus constrained the IR to 267.4 ± 0.4 Ma to 266.5 ± 0.3 Ma based on our estimates. Similarly, Olszewski and Erwin (2009) correlated this interval to the basal Getaway Member, which is the basal HFS G12 in Kerans et al. (2014), and thus estimated to 267.4 ± 0.4 Ma. In general, the IR in West Texas likely took place between the Getaway to basal South Wells members close to the Roadian-Wordian boundary, or between 267.4 ± 0.4 Ma to 266.5 ± 0.3 Ma.

The IR was recognized in the Kyushu Section in Japan, which was correlated to the top fusulinid Assemblage Zone (AZ) of *Neoschwagerina craticulifera* (Kirschvink et al., 2015). This fusulinid AZ was correlated to the late Roadian or the early Wordian (Henderson et al., 2012; Kasuya et al., 2012), and was speculated to occur below the CA-ID-TIMS U-Pb zircon date of 267.46 ± 0.04 Ma at the Shigeyasu Quarry Section in Akiyoshi, Japan (Davydov and Schmitz, 2019), which suggests that the IR might be older than 267.46 ± 0.04 Ma in Japan. The IR was reported in the upper Ecca Group or the lower Beaufort Group in South Africa, and three normal polarity magnetozones N3, N2 and N1 in ascending order was recognized in this interval (Lanci et al., 2013). The magnetozone of N3 was suggested as the IR and estimated around 269 Ma (Roadian) according to the SHRIMP zircon U-Pb dates (268.5 ± 3.5 Ma and 267.1 ± 1.7 Ma) above the magnetozone of N3 (Lanci et al., 2013). Alternatively, Hounslow and Balabanov (2018) suggested that the magnetozones of N1 to N2 might be correlated as the IR, because the SHRIMP zircon U-Pb date of 266.4 ± 1.8 Ma from just below the magnetozone of N2 (Lanci et al., 2013) is close to the estimated age of the IR in West Texas (*e.g.* Henderson et al., 2012). Nevertheless, the SHRIMP zircon U-Pb dates in Lanci et al. (2013) are not accurate or precise enough to figure out whether the onset of the Illawarra Superchron in South Africa is in Roadian or Wordian. Besides, those normal polarity magnetozones might be as old as Kungurian due to the severe Pb-loss in zircons and thus be correlated to the normal polarity wiggles during the Kiaman Superchron (Hounslow and Balabanov, 2018). The IR in its type region of Australia was estimated to be in the Mulbring Siltstone in the Hunter Coal Field of the Sydney

Basin (Menning and Jin, 1998), which has a CA-ID-TIMS U-Pb zircon date of 264.12 ± 0.17 Ma (Laurie et al., 2016). The Mulbring Siltstone correlates to the Broughton Formation of the southern Sydney Basin based on palynological and brachiopod zones (Campbell et al., 2001; Cottrell et al., 2008). The uppermost part of the Broughton Formation has a CA-ID-TIMS U-Pb zircon date of 263.51 ± 0.05 Ma (Metcalfe et al., 2015). A normal polarity magnetozone was reported in the upper Broughton Formation above the Ar-Ar date of 265.05 ± 0.46 Ma and was suggested as the IR (Belica et al., 2017). These dates in Australia are younger than the IR in West Texas, which suggests that the reverse polarity in Australia might be within the Illawarra Superchron instead of the IR.

The IR is well constrained in the upper Urzhumian Stage in Russia, which is widely accepted to be roughly correlated to Wordian (Henderson et al., 2012; Hounslow and Balabanov, 2018; Lucas and Shen, 2018). However, precise correlation remains problematic between the Russian regional stages and the international marine sections with conodont and fusulinid zones. The IR was also reported in the lower part of the Upper Shihhotse Formation in North China, but as the non-marine deposits in North China are poorly dated, the validity of the so-called IR in North China remains controversial (Embleton et al., 1996; Menning and Jin, 1998). Finally, the IR was detected in red-bed successions in Europe with low-resolution biostratigraphy (Hounslow and Balabanov, 2018).

5. Conclusions

Three precise U-Pb CA-ID-TIMS zircon dates of 262.127 ± 0.097 Ma from the Rader Member in the middle Bell Canyon Formation, 264.23 ± 0.13 Ma from the Pinery Member in the lower Bell Canyon Formation, and 266.525 ± 0.078 Ma from the South Wells Member of the upper Cherry Canyon Formation are reported from sections in Guadalupe Mountains National Park. The new geochronology provides high-precision temporal constraints on Guadalupian stage boundaries at their type area. The base Capitanian is interpolated at 264.28 ± 0.16 Ma by the Bayesian age-stratigraphic modeling based on conodont biostratigraphy at the Nipple Hill and the nearby Frijole sections. The Wordian boundary is estimated at 266.9 ± 0.4 Ma based on temporal estimates on the middle Permian HFSs in the Delaware Basin. The end-Guadalupian extinction may have happened within the last 1 myr of the Capitanian and probably continued into the earliest Wuchiapingian. The extinction appears to have been coincident with the peak phase of the ELIP. The conodonts had a distinctly faster evolutionary rate during the extinction interval. Reef ecosystems did not recover until the *Clarkina orientalis* zone (*ca.* 257.8 Ma) in the early Wuchiapingian. The emplacement of ELIP has been constrained to between *ca.* 260 Ma to 257.4 Ma by the associated U-Pb CA-ID-TIMS geochronology, which is consistent with the estimated duration of the conodont ages. From this we conclude that the ELIP may have contributed to the biotic crisis at the end Guadalupian, and could have also hampered the ecosystem restoration in the early Wuchiapingian. The Illawarra Reversal is estimated to between 267.4 ± 0.4 Ma to 266.5 ± 0.3 Ma in West Texas.

Declaration of competing interest

The authors declare that they have no known competing financial interests or personal relationships that could have appeared to influence the work reported in this paper.

Acknowledgements

We thank Spencer Lucas, an anonymous reviewer and editor-in-chief Thomas Algeo for their constructive comments that helped to improve the paper. We acknowledge Guadalupe Mountains National Park for permission to do field work and access to their research facilities and archives. Special thanks to Dr. Jonena Hearst (GMNP) for her guidance and advice in the field. This work is supported by National Natural Science Foundation of China (414201040034, 1830323) and the Strategic Priority Research Programs of the Chinese Academy of Sciences (XDB18000000, XDB26000000).

References

Bagherpour, B., Bucher, H., Schneebeli-Hermann, E., Vennemann, T., Chiaradia, M., Shen, S.Z., 2018a. Early Late Permian coupled carbon and strontium isotope chemostratigraphy from South China: Extended Emeishan volcanism? Gondwana Res. 58, 58–70.
Bagherpour, B., Bucher, H., Yuan, D.X., Leu, M., Zhang, C., Shen, S.Z., 2018b. Early Wuchiapingian (Lopingian, late Permian) drowning event in the South China block suggests a late eruptive phase of Emeishan Large Igneous Province. Glob. Planet. Chang. 169, 119–132.
Baresel, B., Bucher, H., Brosse, M., Cordey, F., Kuang, G.D., Schaltegger, U., 2017. Precise age for the Permian-Triassic boundary in South China from high-precision U-Pb geochronology and Bayesian age-depth modeling. Solid Earth 8 (2), 361–378.
Becker, M.L., Rasbury, E.T., Meyers, W.J., Hanson, G.N., 2002. U-Pb calcite age of the Late Permian Castile Formation, Delaware Basin: a constraint on the age of the Permian-Triassic boundary (?). Earth Planet. Sci. Lett. 203 (2), 681–689.
Belica, M.E., Tohver, E., Pisarevsky, S.A., Jourdan, F., Denyszyn, S., George, A.D., 2017. Middle Permian paleomagnetism of the Sydney Basin, Eastern Gondwana: Testing Pangea models and the timing of the end of the Kiaman Reverse Superchron. Tectonophysics 699 (15), 178–198.
Biakov, A.S., Brynko, I.V., Bond, D.P.G., Harvey, J., Goryachev, N.A., Vedernikov, I.L., Filimonova, T.V., 2019. New minimal $^{87}Sr/^{86}Sr$ values in Permian biogenic carbonates of the Omolon Massif (Northeastern Asia). Dokl. Earth Sci. 488 (2), 1143–1147.
Bond, D.P.G., Hilton, J., Wignall, P.B., Ali, J.R., Stevens, L.G., Sun, Y., Lai, X., 2010a. The Middle Permian (Capitanian) mass extinction on land and in the oceans. Earth Sci. Rev. 102 (1–2), 100–116.
Bond, D.P.G., Wignall, P.B., Wang, W., Izon, G., Jiang, H.S., Lai, X.L., Sun, Y.D., Newton, R.J., Shao, L.Y., Védrine, S., Cope, H., 2010b. The mid-Capitanian (Middle Permian) mass extinction and carbon isotope record of South China. Palaeogeogr. Palaeoclimatol. Palaeoecol. 292 (1), 282–294.
Boven, A., Pasteels, P., Punzalan, L.E., Liu, J., Luo, X., Zhang, W., Guo, Z., Hertogen, J., 2002. $^{40}Ar/^{39}Ar$ geochronological constraints on the age and evolution of the Permo-Triassic Emeishan Volcanic Province, Southwest China. J. Asian Earth Sci. 20 (2), 157–175.
Bowring, S.A., Erwin, D.H., Jin, Y.G., Martin, M.W., Davidek, K., Wang, W., 1998. U/Pb zircon geochronology and tempo of the end-Permian mass extinction. Science 280 (5366), 1039–1045.
Bowring, J.F., McLean, N.M., Bowring, S.A., 2011. Engineering cyber infrastructure for U-Pb geochronology: Tripoli and U-Pb_Redux. Geochem. Geophys. Geosyst. https://doi.org/10.1029/2010GC003479.
Burgess, S.D., Bowring, S.A., Shen, S.Z., 2014. High-precision timeline for Earth's most severe extinction. Proc. Natl. Acad. Sci. 111 (9), 3316–3321.
Campbell, L.M., Conaghan, P.J., Flood, R.H., 2001. Flow-field and palaeogeographic reconstruction of volcanic activity in the Permian Gerringong Volcanic Complex, southern Sydney Basin, Australia. Aust. J. Earth Sci. 48 (3), 357–375.
Cao, C.Q., Cui, C., Chen, J., Summons, R.E., Shen, S.Z., Zhang, H., 2018. A positive C-isotope excursion induced by sea-level fall in the middle Capitanian of South China. Palaeogeogr. Palaeoclimatol. Palaeoecol. 505, 305–316.
Chen, J., Shen, S.Z., 2019. Mid-Permian (End-Guadalupian) extinctions. Reference Module in Earth Systems and Environmental Sciences. https://doi.org/10.1016/B978-0-12-409548-9.11976-1.
Chen, J., Xu, Y.G., 2019. Establishing the link between Permian volcanism and biodiversity changes: Insights from geochemical proxies. Gondwana Res. 75, 68–96.
Chen, B., Joachimski, M.M., Sun, Y.D., Shen, S.Z., Lai, X.L., 2011. Carbon and conodont apatite oxygen isotope records of Guadalupian-Lopingian boundary sections: Climatic or sea-level signal? Palaeogeogr. Palaeoclimatol. Palaeoecol. 311 (3), 145–153.
Chen, B., Joachimski, M.M., Shen, S.Z., Lambert, L.L., Lai, X.L., Wang, X.D., Chen, J., Yuan, D.X., 2013. Permian ice volume and palaeoclimate history: Oxygen isotope proxies revisited. Gondwana Res. 24 (1), 77–89.
Clapham, M.E., Shen, S.Z., Bottjer, D.J., 2009. The double mass extinction revisited: reassessing the severity, selectivity, and causes of the end-Guadalupian biotic crisis (Late Permian). Paleobiology 35 (01), 32–50.
Cohen, K.M., Finney, S.C., Gibbard, P.L., Fan, J.X., 2013. (updated). The ICS International Chronostratigraphic Chart. Episodes 36, 199–204.
Condon, D.J., Schoene, B., McLean, N.M., Bowring, S.A., Parrish, R.R., 2015. Metrology and traceability of U-Pb isotope dilution geochronology (EARTHTIME Tracer Calibration Part I). Geochim. Cosmochim. Acta 164, 464–480.
Cottrell, R.D., Tarduno, J.A., Roberts, J., 2008. The Kiaman Reversed Polarity Superchron at Kiama: Toward a field strength estimate based on single silicate crystals. Phys. Earth Planet. Inter. 169 (1), 49–58.
Davydov, V.I., Crowley, J.L., Schmitz, M.D., Snyder, W.S., 2018a. New U-Pb constraints identify the end-Guadalupian and possibly end-Lopingian extinction events conceivably preserved in the passive margin of North America: implication for regional tectonics. Geol. Mag. 155 (1), 119–131.
Davydov, V.I., Schmitz, M.D., 2019. High-precision radioisotopic ages for the lower Midian (upper Wordian) Stage of the Tethyan time scale, Shigeyasu Quarry, Yamaguchi Prefecture, Japan. Palaeogeogr. Palaeoclimatol. Palaeoecol. 527,

133–145.
Davydov, V.I., Biakov, A.S., Isbell, J.L., Crowley, J.L., Schmitz, M.D., Vedernikov, I.L., 2016. Middle Permian U-Pb zircon ages of the “glacial” deposits of the Atkan Formation, Ayan-Yuryakh anticlinorium, Magadan province, NE Russia: Their significance for global climatic interpretations. Gondwana Res. 38, 74–85.
Davydov, V.I., Biakov, A.S., Schmitz, M.D., Silantiev, V.V., 2018b. Radioisotopic calibration of the Guadalupian (middle Permian) series: Review and updates. Earth Sci. Rev. 176, 222–240.
Day, M.O., Ramezani, J., Bowring, S.A., Sadler, P.M., Erwin, D.H., Abdala, F., Rubidge, B.S., 2015. When and how did the terrestrial mid-Permian mass extinction occur? Evidence from the tetrapod record of the Karoo Basin, South Africa. Proc. R. Soc. B 282, 20150834.
Day, M.O., Benson, R.B.J., Kammerer, C.F., Rubidge, B.S., 2018. Evolutionary rates of mid-Permian tetrapods from South Africa and the role of temporal resolution in turnover reconstruction. Paleobiology 44 (3), 347–367.
Ehiro, M., Shen, S.Z., 2008. Permian ammonoid *Kufengoceras* from the uppermost Maokou Formation (earliest Wuchiapingian) at Penglaitan, Laibin Area, Guangxi Autonomous Region, South China. Paleontol. Res. 12 (3), 255–259.
Embleton, B.J.J., McElhinny, M.W., Ma, X.H., Zhang, Z.K., Li, Z.X., 1996. Permo-Triassic magnetostratigraphy in China: the type section near Taiyuan, Shanxi Province, North China. Geophys. J. Int. 126, 382–388.
Fielding, C.R., Frank, T.D., Isbell, J.L., 2008. The late Paleozoic ice age—A review of current understanding and synthesis of global climate patterns. In: Fielding, C.R., Frank, T.D., Isbell, J.L. (Eds.), Resolving the Late Paleozoic Ice Age in Time and Space. 441. Geological Society of America, pp. 343–354.
Frost III, E.L., Budd, D.A., Kerans, C., 2012. Syndepositional deformation in a high-relief carbonate platform and its effect on early fluid flow as revealed by dolomite patterns. J. Sediment. Res. 82 (12), 913–932.
Glenister, B.F., Boyd, D.W., Furnish, W.M., Grant, R.E., Harris, M.T., Kozur, H.W., Lambert, L.L., Nassichuk, W.W., Newell, N.D., Pray, L.C., Spinosa, C., Wardlaw, B.R., Wilde, G.L., Yancey, T.E., 1992. The Guadalupian: proposed international standard for a middle Permian series. Int. Geol. Rev. 34 (9), 857–888.
Glenister, B.F., Wardlaw, B.R., Lambert, L.L., Spinosa, C., Bowring, S.A., Erwin, D.H., Menning, M., Wilde, G.L., 1999. Proposal of Guadalupian and component Roadian, Wordian and Capitanian stages as international standards for the Middle Permian series. Permophiles 34, 3–11.
Groves, J.R., Wang, Y., 2013. Timing and size selectivity of the Guadalupian (Middle Permian) fusulinoidean extinction. J. Paleontol. 87 (2), 183–196.
Haq, B.U., Schutter, S.R., 2008. A chronology of Paleozoic sea-level changes. Science 322 (5898), 64–68.
Haslett, J., Parnell, A., 2008. A simple monotone process with application to radiocarbon-dated depth chronologies. J. R. Stat. Soc.: Ser. C: Appl. Stat. 57 (4), 399–418.
He, B., Xu, Y.G., Huang, X.L., Luo, Z.Y., Shi, Y.R., Yang, Q.J., Yu, S.Y., 2007. Age and duration of the Emeishan flood volcanism, SW China: Geochemistry and SHRIMP zircon U-Pb dating of silicic ignimbrites, post-volcanic Xuanwei Formation and clay tuff at the Chaotian section. Earth Planet. Sci. Lett. 255 (3–4), 306–323.
Henderson, C.M., 2018. Permian conodont biostratigraphy. Geol. Soc. Lond., Spec. Publ. 450 (1), 119–142.
Henderson, C.M., Mei, S., 2003. Stratigraphic versus environmental significance of Permian serrated conodonts around the Cisuralian-Guadalupian boundary: new evidence from Oman. Palaeogeogr. Palaeoclimatol. Palaeoecol. 191 (3), 301–328.
Henderson, C.M., Davydov, V.I., Wardlaw, B.R., Gradstein, F.M., 2012. Chapter 24 - the Permian Period. In: Gradstein, F.M., Ogg, J.G., Schmitz, M., Ogg, G. (Eds.), The Geologic Time Scale 2012. 1. pp. 653–679 Boston.
Hoke, G.D., Schmitz, M.D., Bowring, S.A., 2014. An ultrasonic method for isolating nonclay components from clay-rich material. Geochem. Geophys. Geosyst. 15 (2), 492–498.
Hounslow, M.W., Balabanov, Y.P., 2018. A geomagnetic polarity timescale for the Permian, calibrated to stage boundaries. Geol. Soc. Lond., Spec. Publ. 450 (1), 61–103.
Huang, H., Cawood, P.A., Hou, M.C., Ni, S.J., Yang, J.H., Du, Y.S., Wen, H.G., 2018. Provenance of Late Permian volcanic ash beds in South China: Implications for the age of Emeishan volcanism and its linkage to climate cooling. Lithos 314–315, 293–306.
Huang, H., Cawood, P.A., Hou, M.C., Yang, J.H., Ni, S.J., Du, Y.S., Yan, Z.K., Wang, J., 2016. Silicic ash beds bracket Emeishan Large Igneous province to <1 m.y. at ~260 Ma. Lithos 264, 17–27.
Huang, Y.G., Chen, Z.Q., Wignall, P.B., Grasby, S.E., Zhao, L.S., Wang, X.D., Kaiho, K., 2019a. Biotic responses to volatile volcanism and environmental stresses over the Guadalupian-Lopingian (Permian) transition. Geology 47 (2), 175–178.
Huang, Y.G., Chen, Z.Q., Zhao, L.S., Stanley, G.D., Yan, J.X., Pei, Y., Yang, W.R., Huang, J.H., 2019b. Restoration of reef ecosystems following the Guadalupian-Lopingian boundary mass extinction: Evidence from the Laibin area, South China. Palaeogeogr. Palaeoclimatol. Palaeoecol. 519 (1), 8–22.
Irving, E., Parry, L.G., 1963. The magnetism of some Permian rocks from New South Wales. Geophys. J. Int. 7 (4), 395–411.
Isozaki, Y., 2009. Illawarra Reversal: the fingerprint of a superplume that triggered Pangean breakup and the end-Guadalupian (Permian) mass extinction. Gondwana Res. 15 (3–4), 421–432.
Isozaki, Y., Kawahata, H., Minoshima, K., 2007. The Capitanian (Permian) Kamura cooling event: The beginning of the Paleozoic-Mesozoic transition. Palaeoworld 16 (1–3), 16–30.
Isozaki, Y., Aljinović, D., Kawahata, H., 2011. The Guadalupian (Permian) Kamura event in European Tethys. Palaeogeogr. Palaeoclimatol. Palaeoecol. 308 (1), 12–21.
Jablonski, D., 1985. Chapter 10 marine regressions and mass extinctions: a test using the modern biota. In: Valentine, J.W. (Ed.), Phanerozoic Diversity Patterns: Profiles in Macroevolution, pp. 335–354 New Jersey.
Jaffey, A.H., Flynn, K.F., Glendenin, L.E., Bentley, W.C., Essling, A.M., 1971. Precision measurement of half-lives and specific activities of U 235 and U 238. Phys. Rev. C 4 (5), 1889–1906.
Jin, Y.G., Zhang, J., Shang, Q.H., 1994. Two phases of the end-Permian mass extinction. Pangea: Global Env. and Resour. 17, 813–822.
Jin, Y.G., Wardlaw, B.R., Glenister, B.F., Kotlyar, G.V., 1997. Permian chronostratigraphic subdivisions. Episodes 20 (1), 10–15.
Jin, Y.G., Shen, S.Z., Henderson, C.M., Wang, X.D., Wang, W., Wang, Y., Cao, C.Q., Shang, Q.H., 2006. The Global Stratotype Section and Point (GSSP) for the boundary between the Capitanian and Wuchiapingian stage (Permian). Episodes 29 (4), 253–262.
Jost, A.B., Mundil, R., He, B., Brown, S.T., Altiner, D., Sun, Y.D., DePaolo, D.J., Payne, J.L., 2014. Constraining the cause of the end-Guadalupian extinction with coupled records of carbon and calcium isotopes. Earth Planet. Sci. Lett. 396, 201–212.
Kani, T., Hisanabe, C., Isozaki, Y., 2013. The Capitanian (Permian) minimum of $^{87}Sr/^{86}Sr$ ratio in the mid-Panthalassan paleo-atoll carbonates and its demise by the deglaciation and continental doming. Gondwana Res. 24 (1), 212–221.
Kasuya, A., Isozaki, Y., Igo, H., 2012. Constraining paleo-latitude of a biogeographic boundary in mid-Panthalassa: Fusuline province shift on the Late Guadalupian (Permian) migrating seamount. Gondwana Res. 21 (2), 611–623.
Kerans, C., Playton, T., Phelps, R., Scott, S.Z., 2014. Ramp to rimmed shelf transition in the Guadalupian (Permian) of the Guadalupe Mountains, West Texas and New Mexico. In: Verwer, K. (Ed.), Deposits, Architecture, and Controls of Carbonate Margin, Slope and Basinal Settings. Special Publication No.105. SEPM Society for Sedimentary Geology, Tulsa, pp. 26–49.
King, B.P., 1948. Geology of the southern Guadalupe Mountains, Texas. Washington, DC: U.S. Geological Survey. Professional Paper 215, 183.
Kirschvink, J.L., Isozaki, Y., Shibuya, H., Otofuji, Y., Raub, T.D., Hilburn, I.A., Kasuya, T., Yokoyama, M., Bonifacie, M., 2015. Challenging the sensitivity limits of Paleomagnetism: Magnetostratigraphy of weakly magnetized Guadalupian-Lopingian (Permian) Limestone from Kyushu, Japan. Palaeogeogr. Palaeoclimatol. Palaeoecol. 418, 75–89.
Klötzli, U., Klötzli, E., Günes, Z., Kosler, J., 2009. Accuracy of laser ablation U-Pb zircon dating: Results from a test using five different reference zircons. Geostand. Geoanal. Res. 33 (1), 5–15.
Korte, C., Jasper, T., Kozur, H.W., Veizer, J., 2006. $^{87}Sr/^{86}Sr$ record of Permian seawater. Palaeogeogr. Palaeoclimatol. Palaeoecol. 240 (1), 89–107.
Kutygin, R.V., Biakov, A.S., 2015. Permian ammonoids of the Okhotsk Region, Northeast Asia. Paleontol. J. 49 (12), 1275–1281.
Lambert, L.L., Wardlaw, B.R., Nestell, M.K., Nestell, G.P., 2002. Latest Guadalupian (Middle Permian) conodonts and foraminifers from West Texas. Micropaleontology 48, 343–364.
Lambert, L.L., Bell, G.L., Fronimos, J.A., Wardlaw, B.R., Yisa, M.O., 2010. Conodont biostratigraphy of a more complete Reef Trail Member section near the type section, latest Guadalupian Series type region. Micropaleontology 56, 233–253.
Lanci, L., Tohver, E., Wilson, A., Flint, S., 2013. Upper Permian magnetic stratigraphy of the lower Beaufort group, Karoo basin. Earth Planet. Sci. Lett. 375, 123–134.
Laurie, J., Bodorkos, S., Nicoll, R., Crowley, J., Mantle, D., Mory, A., Wood, G., Backhouse, J., Holmes, E., Smith, T., 2016. Calibrating the middle and late Permian palynostratigraphy of Australia to the geologic time-scale via U-Pb zircon CA-IDTIMS dating. Aust. J. Earth Sci. 63 (6), 701–730.
Leven, E.Y., Bogoslovskaya, M.F., 2006. The Roadian Stage of the Permian and problems of its global correlation. Stratigr. Geol. Correl. 14 (2), 164–173.
Li, Y.J., He, H.Y., Ivanov, A.V., Demonterova, E.I., Pan, Y.X., Deng, C.L., Zheng, D.W., Zhu, R.X., 2018. $^{40}Ar/^{39}Ar$ age of the onset of high-Ti phase of the Emeishan volcanism strengthens the link with the end-Guadalupian mass extinction. Int. Geol. Rev. 60 (15), 1906–1917.
Liu, X.C., Wang, W., Shen, S.Z., Gorgij, M.N., Ye, F.C., Zhang, Y.C., Furuyama, S., Kano, A., Chen, X.Z., 2013. Late Guadalupian to Lopingian (Permian) carbon and strontium isotopic chemostratigraphy in the Abadeh section, central Iran. Gondwana Res. 24 (1), 222–232.
Lo, C.H., Chung, S.L., Lee, T.Y., Wu, G., 2002. Age of the Emeishan flood magmatism and relations to Permian-Triassic boundary events. Earth Planet. Sci. Lett. 198 (3), 449–458.
Lucas, S.G., 2017. Permian tetrapod extinction events. Earth Sci. Rev. 170, 31–60.
Lucas, S.G., Shen, S.Z., 2018. The Permian chronostratigraphic scale: history, status and prospectus. Geol. Soc. Lond., Spec. Publ. 450 (1), 21–50.
Mattinson, J.M., 2005. Zircon U-Pb chemical abrasion (“CA-TIMS”) method: combined annealing and multi-step partial dissolution analysis for improved precision and accuracy of zircon ages. Chem. Geol. 220 (1), 47–66.
McLean, N.M., Bowring, J.F., Bowring, S.A., 2011. An algorithm for U-Pb isotope dilution data reduction and uncertainty propagation. Geochem. Geophys. Geosyst. https://doi.org/10.1029/2010gc003478.
McLean, N.M., Condon, D.J., Schoene, B., Bowring, S.A., 2015. Evaluating uncertainties in the calibration of isotopic reference materials and multi-element isotopic tracers (EARTHTIME Tracer Calibration Part II). Geochim. Cosmochim. Acta 164, 481–501.
Mei, S.L., Jin, Y.G., Wardlaw, B.R., 1998. Conodont succession of the Guadalupian-Lopingian boundary strata in Laibin of Guagnxi, China and West Texas, USA. Palaeoworld 9, 53–76.
Mei, S.L., Henderson, C.M., Wardlaw, B.R., 2002. Evolution and distribution of the conodonts Sweetognathus and Iranognathus and related genera during the Permian, and their implications for climate change. Palaeogeogr. Palaeoclimatol. Palaeoecol. 180 (1), 57–91.
Mei, S.L., Shi, X.Y., Chen, X.F., Sun, K.Q., Yan, J.X., 1999a. Permian Cisuralian and Guadalupian sequence stratigraphy in south Guizhou and central Guangxi and its relation to conodont evolution. Earth Sci.-J. China Univ. Geosci. 24 (1), 21–31.

Mei, S.L., Zhu, Z.L., Shi, X.Y., Sun, K.Q., Li, B., 1999b. Sequence stratigraphy of Permian Lopingian strata in central Guangxi. Geosciences—J. Graduate School, China Univ. of Geosci. 13 (1), 11–18.
Menning, M., Jin, Y.G., 1998. Comment on 'Permo-Triassic magnetostratigraphy in China: the type section near Taiyuan, Shanxi Province, North China' by B.J.J. Embleton, M.W. McElhinny, X. Ma, Z. Zhang and Z.X. Li. Geophys. J. Int. 133, 213–216.
Metcalfe, I., Crowley, J.L., Nicoll, R.S., Schmitz, M., 2015. High-precision U-Pb CA-TIMS calibration of Middle Permian to Lower Triassic sequences, mass extinction and extreme climate-change in eastern Australian Gondwana. Gondwana Res. 28, 61–81.
Montañez, I.P., Poulsen, C.J., 2013. The Late Paleozoic Ice Age: An evolving paradigm. Annu. Rev. Earth Planet. Sci. 41 (1), 629–656.
Nicklen, B.L., 2011. Establishing a Tephrochronologic Framework for the Middle Permian (Guadalupian) Type Area and Adjacent Portions of the Delaware Basin and Northwestern Shelf, West Texas and Southeastern New Mexico, USA. University of Cincinnati, Cincinmati (119 pp).
Nicklen, B.L., Bell, G.L., Huff, W.D., 2015a. A new shelf-to-basin timeline for the Middle Permian (Guadalupian) Capitan depositional system, west Texas and southeastern New Mexico, USA. Stratigraphy 12 (2), 109–122.
Nicklen, B.L., Bell, G.L., Lambert, L.L., Huff, W.D., 2015b. Tephrochronology of the Manzanita Limestone in the Middle Permian (Guadalupian) Type Area, West Texas and southeastern New Mexico, USA. Stratigraphy 12 (2), 123–147.
Olszewski, T.D., Erwin, D.H., 2009. Change and stability in Permian brachiopod communities from western Texas. PALAIOS 24 (1), 27–40.
Parnell, A.C., Haslett, J., Allen, J.R.M., Buck, C.E., Huntley, B., 2008. A flexible approach to assessing synchroneity of past events using Bayesian reconstructions of sedimentation history. Quat. Sci. Rev. 27 (19), 1872–1885.
Ramezani, J., Bowring, S.A., 2018. Advances in numerical calibration of the Permian timescale based on radioisotopic geochronology. Geol. Soc. Lond., Spec. Publ. 450, 51–60.
Ramezani, J., Schmitz, M.D., Davydov, V.I., Bowring, S.A., Snyder, W.S., Northrup, C.J., 2007. High-precision U-Pb zircon age constraints on the Carboniferous-Permian boundary in the southern Urals stratotype. Earth Planet. Sci. Lett. 256 (1–2), 244–257.
Ramezani, J., Hoke, G.D., Fastovsky, D.E., Bowring, S.A., Therrien, F., Dworkin, S.I., Atchley, S.C., Nordt, L.C., 2011. High-precision U-Pb zircon geochronology of the Late Triassic Chinle Formation, Petrified Forest National Park (Arizona, USA): Temporal constraints on the early evolution of dinosaurs. Geol. Soc. Am. Bull. 123 (11 − 12), 2142–2159.
Retallack, G.J., Metzger, C.A., Greaver, T., Jahren, A.H., Smith, R.M.H., Sheldon, N.D., 2006. Middle-Late Permian mass extinction on land. Geol. Soc. Am. Bull. 118 (11–12), 1398–1411.
Rey, K., Amiot, R., Fourel, F., Rigaudier, T., Abdala, F., Day, M.O., Fernandez, V., Fluteau, F., France-Lanord, C., Rubidge, B.S., Smith, R.M., Viglietti, P.A., Zipfel, B., Lécuyer, C., 2016. Global climate perturbations during the Permo-Triassic mass extinctions recorded by continental tetrapods from South Africa. Gondwana Res. 37, 384–396.
Roberts, N.M.W., Rasbury, E.T., Parrish, R.R., Smith, C.J., Horstwood, M.S.A., Condon, D.J., 2017. A calcite reference material for LA-ICP-MS U-Pb geochronology. Geochem. Geophys. Geosyst. 18 (7), 2807–2814.
Saitoh, M., Isozaki, Y., Yao, J.X., Ji, Z.S., Ueno, Y., Yoshida, N., 2013. The appearance of an oxygen-depleted condition on the Capitanian disphotic slope/basin in South China: Middle-Upper Permian stratigraphy at Chaotian in northern Sichuan. Glob. Planet. Chang. 105, 180–192.
Schmitz, M.D., Davydov, V.I., 2012. Quantitative radiometric and biostratigraphic calibration of the Pennsylvanian-Early Permian (Cisuralian) time scale and pan-Euramerican chronostratigraphic correlation. Geol. Soc. Am. Bull. 124 (3–4), 549–577.
Schmitz, M.D., Kuiper, K.F., 2013. High-precision geochronology. Elements 9 (1), 25–30.
Scotese, C.R., 2014. Atlas of Middle & Late Permian and Triassic Paleogeographic Maps, Maps 43–48 From Volume 3 of the PALEOMAP Atlas for ArcGIS (Jurassic and Triassic) and Maps 49–52 from Volume 4 of the PALEOMAP PaleoAtlas for ArcGIS (Late Paleozoic). Mollweide Projection, PALEOMAP Project, Evanston, IL.
Shellnutt, J.G., Denyszyn, S.W., Mundil, R., 2012. Precise age determination of mafic and felsic intrusive rocks from the Permian Emeishan large igneous province (SW China). Gondwana Res. 22 (1), 118–126.
Shen, S.Z., Ramezani, J., Chen, J., Cao, C.Q., Erwin, D.H., Zhang, H., Xiang, L., Schoepfer, S.D., Henderson, C.M., Zheng, Q.F., Bowring, S.A., Wang, Y., Li, X.H., Wang, X.D., Yuan, D.X., Zhang, Y.C., Mu, L., Wang, J., Wu, Y.S., 2019a. A sudden end-Permian mass extinction in South China. Geol. Soc. Am. Bull. 131 (1–2), 205–223.
Shen, S.Z., Shi, G.R., 2002. Paleobiogeographical extinction patterns of Permian brachiopods in the Asian-western Pacific region. Paleobiology 28 (4), 449–463.
Shen, S.Z., Shi, G.R., 2009. Latest Guadalupian brachiopods from the Guadalupian/Lopingian boundary GSSP section at Penglaitan in Laibin, Guangxi, South China and implications for the timing of the pre-Lopingian crisis. Palaeoworld 18 (2), 152–161.
Shen, S.Z., Xie, J.F., Zhang, H., Shi, G.R., 2009. Roadian-Wordian (Guadalupian, Middle Permian) global palaeobiogeography of brachiopods. Glob. Planet. Chang. 65 (3), 166–181.
Shen, S.Z., Crowley, J.L., Wang, Y., Bowring, S.A., Erwin, D.H., Sadler, P.M., Cao, C.Q., Rothman, D.H., Henderson, C.M., Ramezani, J., Zhang, H., Shen, Y.A., Wang, X.D., Wang, W., Mu, L., Li, W.Z., Tang, Y.G., Liu, X.L., Liu, L.J., Zeng, Y., Jiang, Y.F., Jin, Y.G., 2011. Calibrating the end-Permian mass extinction. Science 334 (6061), 1367–1372.
Shen, S.Z., Cao, C.Q., Zhang, H., Bowring, S.A., Henderson, C.M., Payne, J.L., Davydov, V.I., Chen, B., Yuan, D.X., Zhang, Y.C., Wang, W., Zheng, Q.F., 2013. High-resolution $\delta^{13}C_{carb}$ chemostratigraphy from latest Guadalupian through earliest Triassic in South China and Iran. Earth Planet. Sci. Lett. 375, 156–165.
Shen, S.Z., Zhang, H., Zhang, Y.C., Yuan, D.X., Chen, B., He, W.H., Mu, L., Lin, W., Wang, W.Q., Chen, J., Wu, Q., Cao, C.Q., Wang, Y., Wang, X.D., 2019b. Permian integrative stratigraphy and timescale of China. Science China Earth Sciences 61 (1), 154–188.
Smith, B.P., Larson, T., Martindale, R.C., Kerans, C., 2020. Impacts of basin restriction on geochemistry and extinction patterns: A case from the Guadalupian Delaware Basin, USA. Earth Planet. Sci. Lett. 530, 115876.
Stanley, S.M., Yang, X.L., 1994. A double mass extinction at the end of the Paleozoic Era. Science 266 (5189), 1340–1344.
Steiner, M.B., 2006. The magnetic polarity time scale across the Permian-Triassic boundary. Geol. Soc. Lond., Spec. Publ. 265 (1), 15–38.
Sun, Y.D., Lai, X.L., Wignall, P.B., Widdowson, M., Ali, J.R., Jiang, H.S., Wang, W., Yan, C.B., Bond, D.P., Védrine, S., 2010. Dating the onset and nature of the Middle Permian Emeishan large igneous province eruptions in SW China using conodont biostratigraphy and its bearing on mantle plume uplift models. Lithos 119 (1), 20–33.
Wang, X.D., Sugiyama, T., 2000. Diversity and extinction patterns of Permian coral faunas of China. Lethaia 33 (4), 285–294.
Wang, X.D., Sugiyama, T., 2001. Middle Permian rugose corals from Laibin, Guangxi, South China. J. Paleontol. 75 (4), 758–782.
Wang, W.Q., Garbelli, C., Zheng, Q.F., Chen, J., Liu, X.C., Wang, W., Shen, S.Z., 2018. Permian $^{87}Sr/^{86}Sr$ chemostratigraphy from carbonate sequences in South China. Palaeogeogr. Palaeoclimatol. Palaeoecol. 500, 84–94.
Wardlaw, B.R., Nestell, M.K., 2010. Latest Middle Permian conodonts from the Apache Mountains, West Texas. Micropaleontology 56 (1/2), 149–184.
Wei, H.Y., Wei, X.M., Qiu, Z., Song, H.Y., Shi, G., 2016. Redox conditions across the G-L boundary in South China: Evidence from pyrite morphology and sulfur isotopic compositions. Chem. Geol. 440, 1–14.
Wignall, P.B., Sun, Y., Bond, D.P., Izon, G., Newton, R.J., Védrine, S., Widdowson, M., Ali, J.R., Lai, X., Jiang, H., 2009a. Volcanism, mass extinction, and carbon isotope fluctuations in the Middle Permian of China. Science 324 (5931), 1179–1182.
Wignall, P.B., Védrine, S., Bond, D.P.G., Wang, W., Lai, X.L., Ali, J.R., Jiang, H.S., 2009b. Facies analysis and sea-level change at the Guadalupian-Lopingian Global Stratotype (Laibin, South China), and its bearing on the end-Guadalupian mass extinction. J. Geol. Soc. 166 (4), 655–666.
Wu, Q., Ramezani, J., Zhang, H., Wang, T., Yuan, D.X., Mu, L., Zhang, Y.C., Li, X.H., Shen, S.Z., 2017. Calibrating the Guadalupian series (Middle Permian) of South China. Palaeogeogr. Palaeoclimatol. Palaeoecol. 466, 361–372.
Xu, Y.G., He, B., Luo, Z.Y., Liu, H.Q., 2013. Study on mantle plume and large igneous provinces in China: An overview and perspectives (in Chinese with English abstract). Bull. Mineral. Petrol. Geochem. 32 (1), 25–39.
Yang, J.H., Cawood, P.A., Du, Y.S., Condon, D.J., Yan, J.X., Liu, J.Z., Huang, Y., Yuan, D.X., 2018. Early Wuchiapingian cooling linked to Emeishan basaltic weathering? Earth Planet. Sci. Lett. 492, 102–111.
Yuan, D.X., Shen, S.Z., Henderson, C.M., Chen, J., Zhang, H., Zheng, Q.F., Wu, H.C., 2019. Integrative timescale for the Lopingian (Late Permian): A review and update from Shangsi, South China. Earth Sci. Rev. 188, 190–209.
Zhang, Y.C., Wang, Y., 2018. Permian fusuline biostratigraphy. Geol. Soc. Lond., Spec. Publ. 450 (1), 253–288.
Zhang, G.J., Zhang, X.L., Li, D.D., Farquhar, J., Shen, S.Z., Chen, X.Y., Shen, Y.N., 2015. Widespread shoaling of sulfidic waters linked to the end-Guadalupian (Permian) mass extinction. Geology 43 (12), 1091–1094.
Zhong, Y.T., He, B., Xu, Y.G., 2013. Mineralogy and geochemistry of claystones from the Guadalupian-Lopingian boundary at Penglaitan, South China: Insights into the pre-Lopingian geological events. J. Asian Earth Sci. 62, 438–462.
Zhong, Y.T., He, B., Mundil, R., Xu, Y.G., 2014. CA-TIMS zircon U-Pb dating of felsic ignimbrite from the Binchuan section: Implications for the termination age of Emeishan large igneous province. Lithos 204, 14–19.
Zhong, Y.T., Mundil, R., Chen, J., Yuan, D.X., Denyszyn, S.W., Jost, A.B., Payne, J.L., He, B., Shen, S.Z., Xu, Y.G., 2020. Geochemical, biostratigraphic, and high-resolution geochronological constraints on the waning stage of Emeishan Large Igneous Province. Geol. Soc. Am. Bull. https://doi.org/10.1130/b35464.1.
Zhou, M.F., Malpas, J., Song, X.Y., Robinson, P.T., Sun, M., Kennedy, A.K., Lesher, C.M., Keays, R.R., 2002. A temporal link between the Emeishan large igneous province (SW China) and the end-Guadalupian mass extinction. Earth Planet. Sci. Lett. 196 (3–4), 113–122.